ABSTRACT

Title of Dissertation: **Inferring Radiative Fluxes from a New Generation of Satellites: Model Updates**

Hengmao Wang, Doctor of Philosophy, 2007

Directed By: Dr. Rachel T. Pinker, Professor
Department of Atmospheric and Oceanic Science

In this study an inference scheme is developed to derive surface, Top of the Atmosphere (TOA), and atmospheric spectral shortwave (SW) radiative fluxes for implementation with observations from the Moderate Resolution Imaging Spectroradiometer (MODIS) type of sensors. The model takes into account all atmospheric constituents and addresses the characteristics of water and ice clouds and the variation of cloud particle effective radius. The near infrared spectrum is divided into three bands to better represent the spectral variation of cloud optical properties and water vapor absorption. A multi-layered structure allows for the treatment of surface elevation effects and for the representation of the vertical distribution of the radiative fluxes. Spectral fluxes such as Photosynthetically Active Radiation (PAR) and near-infrared radiation (NIR) are also estimated. The new inference scheme is implemented with MODIS one degree products as well as with the 5 km swath products. The derived fluxes are evaluated against the globally distributed Baseline Radiation Network (BSRN) measurements and compared with products from

independent satellites. It was demonstrated that the MODIS products are in good agreement with ground observations and provide improved estimates of radiative fluxes than the other evaluated satellite products. In problematic areas for most satellite retrievals, such as the Tibet Plateau and Antarctica, the MODIS results have shown a substantial improvement. Availability of the high resolution swath based estimates of surface radiative fluxes allow, for the first time, to address unique space-time coupling issues.

INFERRING RADIATIVE FLUXES FROM NEW GENERATION OF SATELLITES: MODEL UPDATES

By

Hengmao Wang

Dissertation submitted to the Faculty of the Graduate School of the
University of Maryland, College Park, in partial fulfillment
of the requirements for the degree of
Doctor of Philosophy
2007

Advisory Committee:
Dr. Rachel T. Pinker, Chair
Dr. Ernesto Hugo Berbery
Dr. Kaye L. Brubaker
Dr. Allen J. Kaufman
Dr. Daniel Kirk-Davidoff
Dr. Zhanqing Li

Dedication

To my wife Yu, my daughter Sophia born during the writing of this dissertation, my parents and my parents-in-law

Acknowledgements

I would like to express my deepest appreciation to my advisor, Professor Rachel T. Pinker, for her great guidance, continuous support and patience throughout my Ph. D. study at the University of Maryland. My thanks also go to members of my doctoral examination committee for their valuable comments and suggestions on my research work. Very special thanks to Dr. Hongqing Liu, Dr. Jiande Wang, Qing Guo, Bing Yuan and many other friends for their constant encouragement.

I own my deepest gratitude to my wife Yu, my parents, and my parents-in-law for their unconditional support, understanding and love during my studies.

Table of Contents

List of Tables

List of Figures

Chapter 1: Background

Shortwave (SW) radiative fluxes provide the primary forcing of the energy and water budgets in the earth-atmosphere system. Information on the spatial and temporal distribution of such fluxes is required for modeling the hydrologic cycle (Rind et al., 1992; Sorooshian et al., 2002), representing interactions and feedbacks between the atmosphere and the terrestrial biosphere (Dickinson, 1986; Henderson-Sellers, 1993), estimating global terrestrial and oceanic net primary productivity (Running et al., 1999; Platt, 1986), validating climate models (Garrat et al., 1993; Wild et al., 1995; Wielicki et al., 2002), improving the understanding of transport of heat, moisture, and momentum across the surface-atmosphere interface (Sui et al., 2002), improving land-atmosphere interaction parameterizations (Chen et al., 1996), and providing information on the dominant forcing functions of the surface energy budgets (Wood et al., 1997; Rodell et al., 2004). As yet, accurate information on radiative fluxes that will allow addressing all of the above issues is not available from ground observations or numerical models. For example, a comparison of about nineteen General Circulation Models (GCMs) shows a range of 244-267 W/m^2 for global annual means of SW downward fluxes under clear sky conditions and a range of 168-204 W/m^2 for all sky conditions (Wild, 2005). The large discrepancy between SW surface radiation budgets in various GCM models indicates uncertainties in available information on the distribution of solar energy within the climate system and its representation in GCMs. This in turn leads to inaccuracy in the simulation of surface latent and sensible heat fluxes. Reliable information on solar radiation

budgets is needed to better understand processes that determine the utilization of solar energy in the climate system and to improve climate prediction models.

1.1 Current status of surface solar radiation estimates

Surface SW radiative fluxes have been measured by surface radiometers for more than a century. Due to the limited spatial distribution of ground stations and sampling problems inherent with point measurements, those observations lack spatial and temporal coverage. In contrast to surface measurements, satellite observations have the advantage of global coverage. Many attempts have been made to estimate surface SW radiative fluxes from satellite-observed radiances and atmospheric and surface variables at both regional and global scales (Pinker and Ewing, 1985; Ramanathan, 1986; Pinker and Lazlo, 1992; Li and Leighton, 1993; Stephens et al., 1994: Zhang et al., 1995; Gupta et al,. 1999; Mueller et al., 2004; Raschke et al., 1991; Rigollier et al., 2004; Whitlock et al., 1995). Global scale satellite based estimates of such fluxes indicate a scatter. The global mean SW radiation absorbed at the surface as derived from satellite observations by Pinker et al. (1992), Li et al. (1993), and Rossow et al. (1995), are 171.1, 157.0, and 165.1 W/m^2, respectively. The accuracy of the derived values depends on the methodology used, the quality of the satellite data, instrument calibration, the spatial and temporal resolution of the satellite observations that enter the computations, and the spatial and temporal resolution to which these estimates are amalgamated. The need for a systematic evaluation of all of the above issues and their impact on the derived large-scale estimates has been recognized and in 2004 the World Climate Research Program

(WCRP) has established the GEWEX Radiative Flux Assessment (RFA) Working Group to address these issues.

The approach based on satellites observed radiance relate narrowband visible radiance or broadband radiance to radiative fluxes at the surface using radiative transfer parameterization since no reliable information on atmospheric and surface conditions is available from early satellites. The narrowband visible radiance needs to be converted to broadband radiance. Since satellites observe radiances at certain directions, the angular distribution models were performed to obtain radiative fluxes. Both narrow to broadband conversion and angular correction are still not well understood and might bring forth errors into radiative flux estimates. The approaches using atmospheric and surface parameters from satellites retrievals were based on satellites sensors which were not specifically designed for the retrieval of atmospheric and surface parameters.

Most estimates of surface SW radiative fluxes are based on geostationary satellites that have the capability to capture the diurnal variation of clouds. Instruments onboard such satellites have coarse spectral and spatial resolution and thus are limited in their capability to accurately detect cloud or/and aerosol optical properties that are important elements of the radiation budget. The International Satellite Cloud Climatology Project (ISCCP) data (Rossow and Schiffer 1991, 1999) are widely used for inferring radiative fluxes at global scale. The one visible and one infrared channels and coarse spatial resolution of 30 km sampled pixels are not adequate to provide accurate information on optical properties of clouds and aerosols.

The respective inference schemes also require auxiliary information form independent sources. As shown in Table 1.1, to derive radiative fluxes from the ISCCP data, atmospheric humidity from Television and Infrared Observation Satellite (TIROS) Operational Vertical Sounder (TOVS), ozone from Total Ozone Mapping Spectrometer (TOMS), aerosol from Stratospheric Aerosol and Gas Experiment (SAGE), and snow cover from National Oceanic and Atmospheric Administration (NOAA) product are used as auxiliary input parameters. This information is not consistent in space and time with the satellites observations used to derive the solar fluxes. Moreover, geostationary satellites are of limited use at high latitudes due to their restricted viewing geometry.

Table 1.1 Auxiliary data used for cloud retrieval and calculations of radiative fluxes with ISCCP satellite observations

Variables	Data sources for these variables
Cloud cover, optical thickness, top temperature by type	**ISCCP satellite radiances**
Cloud particle size	ISCCP-based climatology
Cloud vertical structure	Combined ISCCP–rawinsonde climatology
Atmospheric temperature and tropospheric humidity	TOVS, Oort climatology for filling
Atmospheric humidity (upper troposphere, stratosphere)	SAGE climatology
Atmospheric composition	Actual record from various sources
Stratospheric total ozone	TOMS, TOVS for filling
Stratospheric ozone profiles	SAGE climatology
Stratospheric aerosols	SAGE
Tropospheric aerosols	Baseline current-day climatology
Snow cover	NOAA product
Sea ice cover	NSIDC product
Diurnal cycle of air temperature over land	Climatology based on surface weather reports and NCEP reanalysis
Surface skin temperature and visible reflectance	From ISCCP retrievals
Surface spectral albedo and emissivity by type	Goddard Institute of Space Studies (GISS) general circulation model reconstruction by surface type and season

1.2 Advantages of MODIS for improving SW radiation budget

Instruments onboard the new generations of sun synchronous satellites tend to have higher spatial and spectral resolution than those on the geostationary satellites, thus improving capabilities to detect atmospheric and surface parameters. The Moderate Resolution Imaging Spectro-radiometer (MODIS) instrument onboard the Terra and Aqua satellites is a state-of-the-art sensor with 36 spectral bands (Table 1.2) with an onboard calibration of both solar and infrared bands. The wide spectral range (0.41-14.24 μm), frequent global coverage (one to two days revisit), and high spatial resolution (250 m for two bands, 500m for five bands and 1000m for 29 bands), permit global monitoring of atmospheric profiles, column water vapor amount, aerosol properties, and clouds, at higher accuracy and consistency than previous Earth Observation Imagers (King *et al*., 1992).

Clouds strongly modulate the energy balance of the earth and the atmosphere through interaction with solar and terrestrial radiation, as demonstrated from both satellite remote sensing (Ramanathan, 1987; Ramanathan et al., 1989) and from models (Ramanathan et al., 1983; Cess et al., 1989). The largest uncertainties in satellite estimates of surface SW fluxes are due to inadequate information on cloud properties such as cloud fraction, cloud optical depth, cloud particle effective radius, cloud thermodynamic phase, and cloud height. Hence, improvements in estimating such fluxes greatly depend on better detection of cloud properties. The MODIS cloud mask is applied globally at single pixel resolution; it uses 17 spectral bands (visible at 250m and infrared at 1000m resolution) to maximize reliable cloud detection and to mitigate past difficulties experienced by sensors with coarser spatial resolution or

with fewer spectral bands (Ackerman et al., 1998). Three carefully chosen bands in the infrared window regions of 8-11 μm and 11-12 μm are

Table 2.1 MODIS spectral band specifications

Primary Use	Band number	Central wavelength [nm]	Bandwidth [nm]	Spatial resolution [m]
Land / Cloud / Aerosols / Boundaries	1	645	620 - 670	250
	2	858.5	841 - 876	
Land / Cloud / Aerosols Properties	3	469	459 - 479	500
	4	555	545 - 565	
	5	1240	1230 - 1250	
	6	1640	1628 - 1652	
	7	2130	2105 - 2155	
Ocean Color / Phytoplankton / Biogeochemistry	8	421.5	405 - 420	1000
	9	443	438 - 448	
	10	488	483 - 493	
	11	531	526 - 536	
	12	551	546 - 556	
	13	667	662 - 672	
	14	678	673 - 683	
	15	748	743 - 753	
	16	869.5	862 - 877	
Atmospheric Water Vapor	17	905	890 - 920	
	18	936	931 - 941	
	19	940	915 - 965	
Surface / Cloud Temperature	20	3750	3660 - 3840	
	21	3959	3929 - 3989	
	22	3959	3929 - 3989	
	23	4050	4020 - 4080	
Atmospheric Temperature	24	4465.5	4433 - 4498	
	25	4515.5	4482 - 4549	
Cirrus Clouds / Water Vapor	26	1375	1360 - 1390	
	27	6715	6535 - 6895	
	28	7325	7175 - 7475	
Cloud Properties	29	8550	8400 - 8700	
Ozone	30	9730	9580 - 9880	
Surface / Cloud Temperature	31	11030	10780 - 11280	
	32	12020	11770 - 12270	
Cloud Top Altitude	33	13335	13185 - 13485	
	34	13635	13485 - 13785	
	35	13935	13785 - 14085	
	36	14235	14085 - 14385	

used to differentiate cloud phase. To-date, no single operational satellite contains three bands within these spectral ranges. Spectral bands, including window regions in the visible and near-infrared, as well as 1.6, 2.1 μm shortwave infrared (SWIR) bands

and 3.7 μm mid-wave infrared (MWIR) bands are used for the retrieval of cloud optical depth and cloud particle effective radius.

It is now well established that natural as well as anthropogenic aerosols affect the global radiation balance by direct and indirect effects. The direct effect refers to the scattering and absorption of radiation by the aerosols (Chylek and Coakley, 1974; Charlson et al., 1992; Penner et al., 1992; Chylek and Wong, 1995). The indirect effect refers to changes in cloud optical properties by aerosols that act as cloud condensation nuclei (CCN) (Twomey, 1977; Lohmann and Lesins, 2002). An increase in aerosols may result in an increase in cloud drop number concentration which, in the absence of absorbing aerosols, leads to higher cloud reflectivity. In recent years, numerous efforts have been undertaken to obtain such information by methods of satellite remote sensing, model simulations, and ground observations. MODIS, with seven channels designed to measure aerosol properties over oceans and three bands over land, can provide more accurate and detailed information on aerosols than previous satellites.

The radiation in the visible part of the spectrum (0.4-0.7 μm), commonly referred to as Photosynthetically Active Radiation (PAR), is required for estimating the net primary productivity over land (Running, 1990) or over oceans (Parslow and Harris, 1990) and for the global scale carbon budget (Bossel, 1996; Leigh, 1999). The partitioning of diffuse and direct PAR is also important for modeling photosynthesis (Gu et al., 2002). The improved information on aerosols and clouds from MODIS

should lead to better estimates of surface spectral radiative fluxes and to a more realistic partitioning into direct and diffuse components.

Polar regions (Arctic and Antarctic) through reflection of incoming solar radiation and the transfer of heat by ocean currents, exert strong influence on the earth's climate, weather patterns and consequently, on the environment. As noted in the Special Report of Regional Impacts of Climate Change (RICC) of International Panel of Climate Change (IPCC) (IPCC, 1998), the Arctic is extremely vulnerable to climate change; major physical, ecological, sociological, and economic impacts are expected. Because of a variety of positive feedback mechanisms, the Arctic is likely to respond rapidly and more severely than any other area on Earth, with consequent effects on sea ice, permafrost and hydrology. Also pointed out in RICC is that changes in polar climate are likely to affect other parts of world through changes in sea level, decreased oceanic heat transport, and increased emissions of green house gases from thawing permafrost. Solar radiative fluxes in polar regions are crucial components of the effort to better understand feedback processes and interactions of climate, hydrology and ecosystem, locally and globally. Surface-based measurements of solar radiation are virtually nonexistent over polar regions which make satellite observations even more critical.

MODIS provides a unique opportunity to derive solar radiation budgets over the polar region. One of the major difficulties over the polar regions is the identification of clouds over snow and ice surfaces because of the low contrast between clouds and snow both in solar wavelengths, due to their similar spectral

albedos, and in terrestrial wavelengths, due to the small temperature difference between the clouds and the surface (in fact, when a temperature difference does exist it very often confuses cloud detection algorithms because the clouds are often warmer than the surface). MODIS currently applies up to six separate spectral threshold tests over snow and ice surfaces during daytime, which leads to improved accuracies in differentiating clouds from snow; only two bands are used for preparing the ISCCP data (0.6 and 1.1 μm) and five bands for the AVHRR (Advanced Very High Resolution Radiometer). Moreover, MODIS on board Terra and Aqua provide multiple views from polar passes at high latitude. As shown in Figure 1, the combination of the two satellites enables to capture the diurnal variation of atmospheric condition (Key et al., 2002). Therefore, over polar regions, diurnally representative estimates of surface solar radiation budget can be derived from MODIS observations.

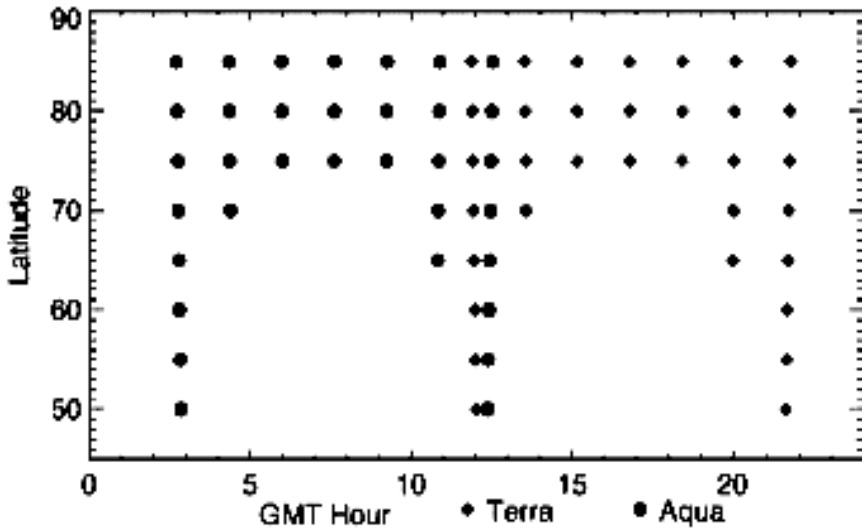

Figure 1.1 Successive overpasses of both Terra and Aqua as a function of latitude over the course of a 24-hour period at the Prime Meridian on September 2000. Only overpasses with sensor view angles less than 50 are considered (Key *et al*., 2002).

1.3 Need for high resolution radiative fluxes

The ability to derive radiative fluxes at global scale from the same high quality instrument is important for many new research initiatives. For example, under the Coordinated Enhanced Observing Period (CEOP) activity (Grassl, 2002) that started in the summer of 2001, issues to be addressed include those related to water and energy fluxes over land areas, monsoonal circulations, extension of derived products from operational satellites (e.g., ISCCP), the Global Precipitation Climatology Project (GPCP), Surface Radiation Budget (SRB), Global water Vapor Project (GVaP), International Satellite Land Surface Climatology Project (ISLSCP)) and validation of products from new satellite systems. Under CEOP, simultaneous observations are collected over several Global Energy and Water Cycle Experiment (GEWEX) Continental Scale Experiment (CSE) sites, as well as over additional regions of climatic significance. This should provide an opportunity to evaluate the usefulness of ongoing operational satellites and new generation experimental satellites in hydrological research, and to improve Numerical Weather Prediction (NWP) and climate predictions. The radiative fluxes derived from MODIS could serve as a calibration reference for estimates derived from other satellites, and help to establish limits on the accuracy at which radiative fluxes can be estimated.

It is of importance to utilize MODIS observations (that provide improved description of atmospheric and surface conditions than previous satellites) to evaluate the performance of algorithms that were originally designed for satellite observations with limited capabilities to derive information on clouds and aerosols. To enable the use of independently derived optical parameters from multi-spectral satellite

observations, the University of Maryland (UMD)/Shortwave Radiation Budget (SRB) model (Pinker and Ewing, 1985; Pinker and Lazlo, 1992; Pinker et al., 2003), has been modified for use with such observations and tested with MODIS based parameters. The modified version (UMD/SRB_M) model uses a pre-calculated look-up table to calculate radiative fluxes. This approach is fast for computing and convenient for the implementation of the model at near real-time and at large scale. Nevertheless, the configuration of look-up tables makes it difficult to incorporate more variables such as cloud particle effective radius and cloud location. Introduction of additional variables will enlarge the look-up table and slow down the search. A new inference scheme is developed to estimate surface, TOA, and atmospheric absorption of shortwave radiation from the detailed information on cloud and aerosol propertied from the unique observations now available from MODIS, both on Terra and Aqua platforms.

The new model (UMD/MODIS) is based on the delta-Eddington approximation to solve radiative transfer equations. Compared to the original UMD/SRB model, the new model takes into account both water and ice clouds and their corresponding optical properties through the adoption of new cloud parameterization schemes. One single near-infrared band in the UMD/SRB model was expanded to three bands in the new version so that characterization of spectral change of water absorption and cloud optical properties could be improved. The earlier parameterization of water vapor absorption was replaced by a scheme based on a more extensive spectroscopic database and incorporates the water vapor continuum model. The aerosol models ware updated to include more aerosol types. In

addition, the layered structure of the new inference scheme facilitates the treatment of surface elevation effects. The forward approach of the new inference scheme avoids the previously required narrow to broadband conversion and angular correction and utilizes all relevant MODIS based information.

A detailed description of the new model is presented in Chapter 2. Preliminary test results are discussed in Chapter 3. The new model is implemented both with gridded MODIS products at 1^0 and with swath products at 5 km resolution. The derived radiative fluxes are compared with those derived from ISCCP by UMD/SRB and GISS models and evaluated against ground measurements. The results and analyses are shown in Chapter 4. A summary and conclusions from this study are given in Chapter 5.

Chapter 2: Model configuration

The new inference scheme is based on the delta-Eddington approximation to solve the radiative transfer equations (Wiscombe, 1977). The model calculates SW radiative fluxes for a plane-parallel, vertically inhomogeneous, scattering and absorbing atmosphere in seven spectral intervals (0.2-0.4, 0.4-0.5, 0.5-0.6, 0.6-0.7, 0.7-1.19, 1.19-2.38, 2.38-4.0 μm) at specified pressure levels. The radiative transfer model accounts for absorption by ozone and water vapor, multiple scattering by molecules, multiple scattering and absorption by aerosols and cloud droplets, and multiple reflection between the atmosphere and surface. The atmosphere is divided into more than 30 layers, depending on the chosen aerosol profiles and on the presence of clouds and cloud layers. The vertical profiles of ozone and water vapor densities, temperature, and pressure are those of the standard atmospheres (tropical, midlatitude summer and winter, subarctic winter and summer) (Kneizys et al., 1980). The new inference scheme consists of two parts: Optical Properties Solver and Radiative Transfer Solver. The parameterizations used in the new inference scheme are described in what follows.

2.1 Relevant parameterizations

2.1.1 Ozone absorption

Ozone absorbs solar radiation in the ultraviolet (Hartley and Huggins band) and in the visible (Chappuis band). The fraction of incident solar radiation absorbed by ozone is computed following Lacis and Hansen (1974):

$$A_{UV} = \frac{1.082x}{(1+138.6x)^{0.805}} + \frac{0.0658x}{1+(103.6x)^3} \qquad (2.1.1)$$

$$A_{VIS} = \frac{0.02118x}{1+0.042x+0.000323x^2} \qquad (2.1.2)$$

where A_{UV} and A_{VIS} are the fraction of radiation absorbed over ultraviolet (0.2-0.4) and visible (0.5-0.6 and 0.6-0.7 um) region, respectively, and x is the effective ozone amount given as:

$$x = uM \qquad (2.1.3)$$

u is the ozone amount in a vertical column and M is a magnification factor defined as:

$$M = \frac{35}{(1223\mu^2+1)^{1/2}} \qquad (2.1.4)$$

where μ is the cosine of the solar zenith angle.

2.1.2 Water vapor absorption

The parameterization of water vapor absorption follows the k-distribution method proposed by Chou and Lee (1996) and further advanced by Tarasova and Fomin (2000). The transmission between the top of atmosphere and pressure level p′ is given as:

$$\tau_\nu(p) = e^{-1/g(\mu_0)\int_0^p k_\nu(p',T')q(p')dp'} \qquad (2.1.5)$$

where ν is the wave-number, μ_0 is the cosine of the solar zenith angle, k_ν is the absorption coefficient, T′ is the temperature, q is the specific humidity, and g is the gravitational acceleration. The variation of k with ν depends strongly on pressure but

weakly on temperature. The effect of pressure and temperature is taken in account by using the one-parameter scaling for the absorption coefficient:

$$k_\nu(p,\theta) = k_\nu(p_r,\theta_r)\left(\frac{p}{p_r}\right)^m f(\theta,\theta_r) \qquad (2.1.6)$$

where p_r is the reference pressure, θ_r is the reference temperature, m is empirical constant less than 1 and f (θ, θ_r) is the temperature scaling function. It has been found by Chou (1986) that the solar fluxes can be computed accurately by choosing p_r =300 hPa and m=0.8. The temperature scaling function for water vapor is given as:

$$f(\theta,\theta_{r)} = 1 + 0.00135(\theta - \theta_r) \qquad (2.1.7)$$

Using the scaling approximation of the absorption coefficient, the mean transmission of atmospheric layer with constant pressure and temperature over a narrow spectral interval $\Delta\nu_i$, can be written as:

$$T_i = \frac{1}{\Delta\nu_i}\int_{\Delta\nu_i} e^{-k_\nu(p_r,\theta_r)w(p,\theta)/\mu_0}\,d\nu \qquad (2.1.8)$$

The scaled water vapor *w (p, θ)* is given as:

$$w(p,\theta) = w'\left(\frac{p}{p_r}\right)^m f(\theta,\theta_r) \qquad (2.1.9)$$

where w' is the water vapor amount in the atmospheric layer. Thus, the scaling of the absorption coefficient is reduced to the scaling of water vapor amount. The integration over wave-numbers can be replaced by the integration over k-intervals using the k-distribution method:

$$T_i = \sum_{j=1}^{n} f_i(k_j)e^{-k_j w(p,\theta)/\theta_0} \qquad (2.1.10)$$

where n is the number of k-intervals, $f_i(k)$ is the k-distribution function in the interval *i* for $p_r = 300mb$, and $\theta_r = 240K$.

Solar fluxes over a wide spectral interval can be computed from:

$$F = \mu_0 \sum_i (S_i \Delta \nu_i) T_i(w(p,\theta), \mu_0) = S_0 \mu_0 \sum_j^n e^{-k_j w(p,\theta)/\mu_0 \Delta g_j} \quad (2.1.11)$$

where S_0 is the total extraterrestrial solar flux, $S_i \Delta \nu_i$ are the solar fluxes in the spectral interval I, and Δg_j is the flux-weighted k-distribution function given by:

$$\Delta g_j = \sum_i (S_i \Delta \nu_i) f_i(k_j) / S_0 \quad (2.1.12)$$

The k-distribution function $f_i(k)$ is derived from a high spectral resolution spectroscopic database. Tarasova and Fomin (2000) advanced the k-distribution method proposed by Chou and Lee (1996) by using more complicated High-Resolution Transmission molecular absorption (HITRAN-96) spectroscopic database (Rothman et al., 1998) and the water vapor continuum model (Clough et al., 1989). The flux-weighted k-distribution function over four spectral intervals is given in Table-2.1.

2.1.3 Rayleigh Scattering

Molecular scattering (Rayleigh) in the atmosphere is considered for all seven spectral intervals. For Rayleigh scattering, single scattering albedo ϖ=1 and asymmetry factor g=0. The Rayleigh scattering optical depth of a layer dτ between level l and l-1 (Penndorf, 1957), is given as:

$$d\tau = 27.019t\left[1 + \frac{0.5(z_{l-1} + z_l)}{6371}\right]^2 \frac{(1 + 29/18r)}{(1+r)(p_l - p_{l-1})} \quad (2.1.13)$$

where z_l and z_{l-1} are heights (km) at level l and l-1, p_l and p_{l-1} are pressures (mb) at level l and l-1, r is the relative humidity and t is a function of wavelength, depolarization factor, and refractive index of the air. Corrections for humidity and the variation of gravity with altitude are included. The parameter t for the seven spectral intervals was computed with the Atmospheric Radiation (ATRAD) model (Wiscombe et al. 1984).

Table 2.1 The flux-weighted k-distribution function, Δg in four spectral intervals for $p_r = 300mb$ and $\theta_r = 240\,\mathrm{K}$. Parameter k is the absorption coefficient ($g^{-1}cm^2$)

n	K	0.55-0.7 μm	0.7-1.19 μm	1.19-2.38 μm	2.38-4.0 μm
0	0.0000	0.73320			
1	0.0010	0.21966	0.60239	0.41872	0.10018
2	0.0133	0.02461	0.17831	0.11855	0.15838
3	0.0422	0.01389	0.065137	0.048076	0.1306
4	0.1334	0.006908	0.075077	0.10376	0.14987
5	0.4217	0.000796	0.043753	0.067603	0.12024
6	1.3340	0.000208	0.018141	0.083264	0.065726
7	5.6230	0.000176	0.007681	0.12142	0.073372
8	31.620	0.000158	0.005084	0.016024	0.069275
9	177.8	0.0000855	0.003149	0.017946	0.11336
10	1000.0		0.001282	0.005542	0.018996

2.1.4 Water cloud parameterization

For water cloud absorption and scattering, the radiative parameterization of

Edwards and Slingo (1996) is employed. In this approach the optical properties of water clouds are represented in terms of liquid water path (LWP) and effective cloud droplet radius (r_e). LWP (gm^{-2}) and r_e (μm) are defined as follows:

$$LWP = \int_{base}^{top} LWC dz \qquad (2.1.14)$$

$$r_e = \int_0^\infty n(r) r^3 dr \Big/ \int_0^\infty n(r) r^2 dr \qquad (2.1.15)$$

where LWC is the liquid water content ($g\ m^{-3}$) at height z (m), r is the droplet radius (μm) and n(r) is the droplet size distribution functions. For a given spectral interval i, the single scattering properties of water clouds (Slingo, 1986) are given as:

$$\tau_i = LWP\left(a_i + \frac{b_i}{r_e}\right) \qquad (2.1.16)$$

$$1 - \omega_i = c_i + d_i . r_e \qquad (2.1.17)$$

$$g_i = e_i + f_i . r_e \qquad (2.1.18)$$

where τ_i is the cloud optical depth, ω_i is the single scattering albedo g_i is the asymmetry parameter, and a_i-f_i are coefficients.

These parametrizations are based on comprehensive Mie calculations using analytical size distributions with effective radii in the range of 3-24 μm. Calculations were performed at 128 wavelength from 0.2 to 200 μm. The derived single scattering properties were averaged over each of the specified spectral bands, weighted by the solar spectrum and radiative propertied of optically thick clouds; the coefficients *a-f* were obtained by fitting the cloud droplet effective radius to the average optical properties. Table 3 contains coefficients for the Edwards-Slingo parameterization for liquid water clouds.

Table 2.2 The coefficients in the parameterization of the optical properties of water droplets for the 4-band scheme as given by Slingo (1989), as derived using thick averaging (Edwards and Slingo, 1996). The coefficients are given in SI units

Band (μm)	a	b	c	d	e	f
0.25-0.69	-8.737×10^{0}	1.671×10^{-3}	7.465×10^{-8}	1.114×10^{-1}	8.371×10^{-1}	1.729×10^{3}
0.69-1.19	-1.451×10^{1}	1.772×10^{-3}	6.745×10^{-6}	9.879×10^{0}	8.144×10^{-1}	2.642×10^{3}
1.19-2.38	-2.576×10^{1}	1.959×10^{-3}	1.278×10^{-3}	6.149×10^{2}	7.914×10^{-1}	3.701×10^{3}
2.38-4.0	-3.414×10^{1}	2.147×10^{-3}	6.067×10^{-2}	7.566×10^{3}	8.354×10^{-1}	3.503×10^{3}

2.1.5 Ice cloud parameterization

Ice clouds occur globally and at all times of the year, covering up to 40% of the earth (Wylie *et al*., 1994). The microphysical and optical properties of ice clouds are far more complicated than those of water clouds, due primarily to the non-sphericity of the ice crystals. The parameterization of ice cloud optical properties developed by Chou et al (2002) was applied in the UMD/MODIS inference scheme where the bulk optical properties of ice clouds such as extinction coefficient, single scattering albedo and asymmetry factor, are given as a function of the effective particle size of a mixture of ice habits, the ice water amount, and spectral band:

$$\beta = a_0 / D_e \qquad (2.1.19)$$

$$1 - \omega = b_0 + b_1 D_e + b_2 D_e^2 \qquad (2.1.20)$$

$$g = c_0 + c_1 D_e + c_2 D_e^2 \qquad (2.1.21)$$

where β is the mass extinction coefficient, ω is single scattering albedo, g is asymmetry factor, a, b, and c are regression coefficients and D_e is effective particle size of a cloud layer with a mixture of various habits and sizes and defined as:

$$D_e = \frac{3}{2}\frac{V}{A} = \frac{3}{2}\frac{C}{\rho_{ice} A} \tag{2.1.22}$$

where C is the concentration of ice particles in mass per unit volume, $\rho_{ice} = 0.92$ g cm^{-3} id the density of ice, A is the total projected area of the particles per unit volume of air, and V is the mixing ratio of ice particle by volume given by:

$$A = \int \left[\sum_i A_i(L) f_i(L) \right] n(L) dL \tag{2.1.23}$$

$$V = \int \left[\sum_i V_i(L) f_i(L) \right] n(L) dL \tag{2.1.24}$$

where i denotes the habit, A_i is the projected area of a particle perpendicular to the light when randomly oriented in space, V_i is the mixing ratio of ice particle by volume, f_i (L) is the particle number distribution-density function for the size L and the habit i.

The Chou et al (2002) parameterization of the bulk optical properties of ice clouds is based on single-scattering optical properties of individual ice particles as a function of particle habit, particle size, and wavelength as computed by Yang et al. (2000) using the improved geometric optics method, namely, the light scattering by non-spherical ice crystals is solved by a ray tracing method. In this technique, the total electric and magnetic fields at the particle surface are computed using the geometric reflection and refraction rays as well as the incident field. For 30 sample cirrus clouds, which are identified by a particle size distribution, a composition of particle habits and the aspect ratios of particle size dimension, the mean effective particle size, mass absorption coefficient, single scattering albedo and asymmetry

factor are computed. The bulk optical properties are then parameterized as a function of the mean effective particle size. Table 3 shows the coefficients for the parameterization for ω and g. It is noted that for the parameterization for extinction coefficient β, coefficient a_0 equals 3.267 m^2g^{-2} μm for all bands.

Table 2.3 Coefficients in the ice cloud parameterization for ω and g. The coefficients are given in SI units

Band (μm)	b_0	b_1	b_2	c_0	c_1	c_2
0.31-0.4	1.37e-07	7.06e-08	5.64e-12	7.56e-01	1.08e-03	-4.21e-06
0.4-0.7	-1.52e-07	7.38e-08	-3.48e-11	7.46e-01	1.41e-03	-5.74e-06
0.7-1.22	1.41e-06	5.72e-06	-1.22e-09	7.25e-01	1.85e-03	-7.73e-06
1.22-2.27	1.12e-03	5.65e-04	-8.96e-07	7.17e-01	2.28e-03	-8.86e-06
2.27-4.0	4.83e-02	2.74e-03	-9.02e-06	7.71e-01	2.45e-03	-1.00e-05

2.1.6 Aerosols

The single scattering properties and vertical profiles of aerosols were derived from the Optical Properties of Aerosols and clouds (OPAC) software package (Hess et al., 1998). Five atmospheric aerosol profiles (Continental, Desert, Maritime, Arctic and Antarctic) are applied with the inference scheme. The aerosol types used describe typical aerosol optical properties over anthropogenically influenced continental areas, deserts, maritime environment, Arctic and Antarctic. The atmosphere is divided into three layers, as shown in Table 2.4. For each layer, the extinction coefficient, single scattering albedo and asymmetry factor are given as a function of wavelength and aerosol type. The optical properties in the seven spectral bands of the inference

scheme were calculated from OPAC output for 24 spectral intervals ranging from 0.25-4.0 μm:

$$\sigma_{\Delta\lambda} = \frac{\int_{\Delta\lambda} \sigma_\lambda E_\lambda d\lambda}{\int_{\Delta\lambda} E_\lambda d\lambda} \qquad (2.1.25)$$

$$\omega_{\Delta\lambda} = \frac{\int_{\Delta\lambda} \omega_\lambda \sigma_\lambda E_\lambda d\lambda}{\int_{\Delta\lambda} \sigma_\lambda E_\lambda d\lambda} \qquad (2.1.26)$$

$$g_{\Delta\lambda} = \frac{\int_{\Delta\lambda} g_\lambda \sigma_\lambda E_\lambda d\lambda}{\int_{\Delta\lambda} \sigma_\lambda E_\lambda d\lambda} \qquad (2.1.27)$$

where σ, ω and g are extinction coefficient, single scattering albedo and asymmetric factor respectively; E_λ is the extraterrestrial spectral irradiance.

Table 2.4 Height profiles of aerosol types from OPAC

Aerosol type	H (km)	Z (km)	H_{ft} (km)
Continent	2	8	10
Maritime	2	1	10
Desert	6	2	6
Arctic	2	99	10
Antarctic	10	8	2
Free atmosphere H_{ft} variable		8	
Stratosphere (12-35 km)	23	99	

2.2 Cloud base height

Visible and infrared satellite sensors are limited to the retrieval of information from the utmost cloud layer or column-integral properties. MODIS provides only cloud top height and currently, no information is available on cloud base height. A statistical model of global cloud layer thickness (Wang et al., 2000) was employed to obtain vertical profiles of radiative fluxes. This statistical model is based on 20 years of global rawinsonde humidity profiles. Cloud layers are identified by relative humidity threshold values of 85%, while the maximum relative humidity within the cloud must be at least 87%. Cloud layer top and base are identified by relative humidity jumps greater than 3%. The relative humidity threshold is based on comparisons of rawinsonde humidity profiles with aircraft observations of cloud top and base heights (Poore et al., 1995) and surface estimates of cloud base heights (Wang and Rossow, 1995). The relative humidity profile is examined sequentially from the surface to the top to find cloud bases and tops. The obtained 20 years cloud layer thickness climatology was fitted to cloud top pressure, latitude and month of the year for land and ocean. This statistical model provides cloud layer thickness as a function of cloud top pressure, latitude and month of year for land and ocean separately.

2.3 Optical properties solver

Using radiative parameterization schemes, with atmospheric and surface properties from satellite observations, the optical properties solver sets up the computational layers, determines the extinction optical depth, single scattering albedo and asymmetry factor of every atmospheric layer and prepares all the necessary information for deriving SW radiative fluxes. The bulk optical properties for each

spectral interval and each atmospheric layer are calculated following Leighton (1979):

$$\tau = \sum_i \tau_i \tag{2.3.1}$$

$$\omega = \frac{\sum_i \omega_i \tau_i}{\tau} \tag{2.3.2}$$

$$g = \frac{\sum_i g_i \omega_i \tau_i}{\omega_i \tau_i} \tag{2.3.3}$$

where the subscript i refers to various radiatively important constituents. The flowchart of the optical properties solver is shown in Figure 2.1.

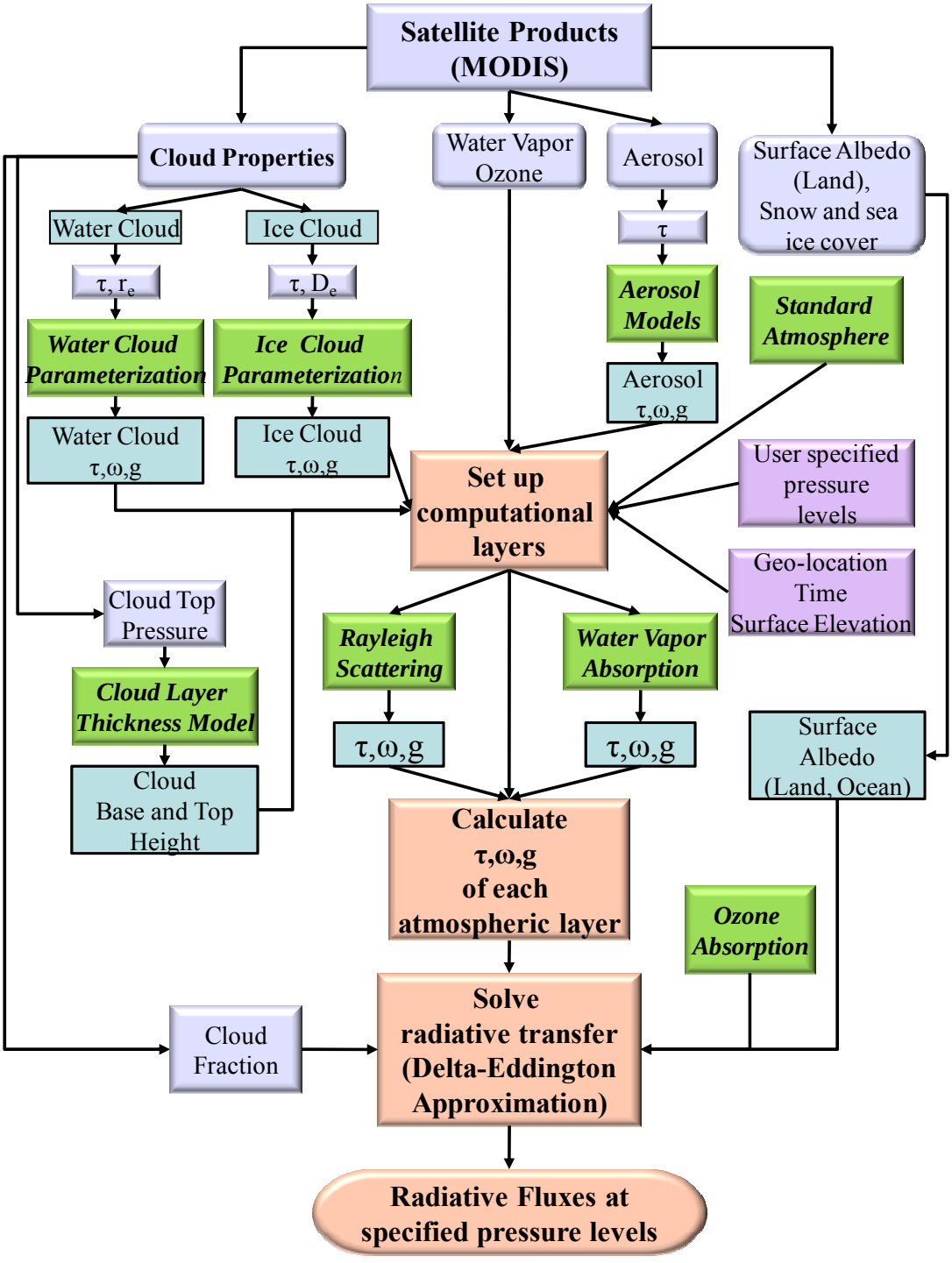

Figure 2.1 Flowchart of the new UMD/MODIS inference scheme

2.4 Radiative transfer solver

The radiative fluxes are calculated using delta-Eddington approximation for a vertically inhomogeneous atmosphere (Wiscombe, 1977). The general equation for absorption and scattering of solar radiation in a plane-parallel atmosphere for each wavelength interval can be written as:

$$\mu \frac{dI(\tau,\mu)}{d\tau} = I(\tau,\mu) - \frac{\omega(\tau)}{2}\int_{-1}^{1} d\mu' p(\mu,\mu') I(\tau,\mu') - \frac{\omega(\tau) I^0}{4\pi} p(\mu,\mu_0) e^{-\tau/\mu_0} \quad (2.4.1)$$

where I is the mean radiance, τ is the optical depth, ω is the single scattering albedo (ratio of scattering extinction to total extinction), p is the scattering phase function, μ is the cosine of the zenith angle, μ_0 is the cosine of the zenith angle for the direct solar beam, and I^0 is the mean radiance at the upper boundary of the model. The scattering phase function p is a non-dimensional quantity that describes the probability of angular distribution of the scattered energy. The first moment of the phase function is the asymmetry factor g, which gives the overall directionality of the phase function. The first term in the right-hand side of Equation 2.4.1 represents attenuation by absorption, the second term represents the diffusive radiation increase by multiple scattering, and the last term is the contribution from single-scattering of the direct solar beam.

Before obtaining a solution of Equation 2.4.1 with a two-stream method, delta scaling of the optical parameters for cases of highly anisotropic phase functions is necessary to improve the accuracy of the solution as proposed in Joseph et al. (1976):

$$g' = \frac{g}{1+g} \tag{2.4.2}$$

$$\tau' = (1 - \omega.g^2).\tau \tag{2.4.3}$$

$$\omega' = \frac{(1-g^2).\omega}{1-\omega.g^2} \tag{2.4.4}$$

This is done to reduce the anisotropy caused by the strong forward-scattering peak characteristic of larger particles (aerosols and clouds).

For the two-stream method, the diffuse radiance is divided into up-welling and down-welling components, I^+ and I^-, respectively. The Eddington approximation gives the phase function and intensity values as follows:

$$I^{\pm}(\tau) = I_0(\tau) \pm \mu I_1(\tau) \tag{2.4.5}$$

$$p(\mu, \mu') = 1 + 3g\mu\mu' \tag{2.4.6}$$

For the Eddington approximation, the fluxes may be calculated as:

$$F^+ = \int_0^{2\pi}\int_0^1 I(\tau,\mu)\mu d\mu d\varphi = 2\pi\mu_1 I^+ \tag{2.4.7}$$

$$F^- = 2\pi\mu_1 I^- \tag{2.4.8}$$

This produces a pair of flux equations from Eq. 2.4.1 (Meador and Weaver, 1980):

$$\frac{dF^+}{d\tau} = \gamma_1 F^+ - \gamma_2 F^- - F^0 \omega\gamma_3 e^{-\tau/\mu_0} \tag{2.4.9}$$

$$\frac{dF^-}{d\tau} = \gamma_2 F^+ - \gamma_1 F^- + F^0 \omega(1-\gamma_3) e^{-\tau/\mu_0} \tag{2.4.10}$$

where F^0 is the direct solar flux at the upper boundary of atmospheric layers, the coefficients of the fluxes equations are given as:

$$\lambda_1 = \frac{1}{4}[7 - \omega(4 + 3g)] \tag{2.4.11}$$

$$\lambda_2 = -\frac{1}{4}[1 - \omega(4 - 3g)] \tag{2.4.12}$$

$$\lambda_3 = \frac{1}{4}(2 - 3g\mu_0) \tag{2.4.13}$$

The solutions to equations 2.4.9 and 2.4.10 are given as:

$$F^+ = vKe^{k\tau} + uHe^{-k\tau} + \varepsilon e^{-\tau/\mu_0} \tag{2.4.14}$$

$$F^- = uKe^{k\tau} + vHe^{-k\tau} + \gamma e^{-\tau/\mu_0} \tag{2.4.15}$$

where

$$k^2 = \gamma_1^2 - \gamma_2^2 \tag{2.4.16}$$

$$v = \frac{1}{2}[1 + (\gamma_1 - \gamma_2)/k] \tag{2.4.17}$$

$$u = \frac{1}{2}[1 - (\gamma_1 - \gamma_2)k] \tag{2.4.18}$$

$$\varepsilon = [\gamma_3(1/\mu_0 - \gamma_1) - \gamma_2(1 - \gamma_3)]\mu_0^2\omega F^0/(1 - \mu_0^2k^2) \tag{2.4.19}$$

$$\gamma = -[(1 - \gamma_3)(1/\mu_0 + \gamma_1) + \gamma_2\gamma_3]\mu_0^2\omega F^0/(1 - \mu_0^2k^{2)} \tag{2.4.20}$$

The coefficients K and H are determined from the boundary conditions that no diffuse radiation is incident at the top of the atmosphere, while at the bottom of the atmosphere (the Earth's surface), radiation is reflected isotropically with a known albedo. Each atmospheric layer is taken as internally homogeneous with specified

vertical optical depth, single scattering albedo, and asymmetry factor. Given N atmospheric layers, there will be 2*N linear equations for unknown constants (2 for each layer).

2.5 Evaluation and Sensitivity Tests

The accuracy of the new inference scheme is evaluated against a high-resolution sophisticated radiative transfer model. A well-known and widely used version of the discrete ordinate model (DISORT) (Stamnes et al., 1988), namely, the Santa Barbara Discrete ordinate Atmospheric Radiative Transfer Model (SBDART) was chosen for comparison with the new inference scheme. SBDART combines the sophisticated discrete ordinate radiative transfer module, low-resolution atmospheric transmission model, and Mie scattering for light scattering by water droplets and ice crystals. With same input parameters, surface downward shortwave total and diffuse fluxes are computed from both the new inference scheme and SBDART for clear and cloudy conditions. SBDART is run with four streams at 0.005 μm resolution.

2.5.1 Clear Sky

The clear sky case evaluated is specified as a cloud free mid-latitude atmosphere with: cosine of solar zenith angle=-0.5, aerosol optical depth=0.2, precipitable water=0.14 cm, total zone amount=0.25 cm, surface albedo=0.2 and surface elevation =0.0 km. To examine the sensitivity of derived fluxes to these parameters, computations are done by varying one parameter at a time while keeping the other five constant. In Figure 9 shown are evaluation results for clear sky conditions. The difference between the new inference scheme and SBDART is

examined by the relative difference defined as the percentage of the difference of the two models to the mean of the SBDART results.

Figure 2.2 shows the comparison between the new inference scheme (UMD/MODIS) and SBDART for clear conditions. As cosine of solar zenith angle changes from 0.1 to 1.0, total and diffuse fluxes calculated by the new inference scheme follow closely the SBDART results. The relative difference is just 0.7% for the total and 1.0% for the diffuse flux. The broadband water vapor parameterization yields satisfactory results when compared with SBDART's high spectral resolution treatment. The new inference scheme slightly underestimates the water vapor absorption, having a relative difference of 0.8% and 1.2% for total and diffuse flux respectively. The absorption by ozone is also underestimated. The relative difference for ozone absorption is 0.9% for total and 1.3% for diffuse flux.

For aerosol radiative effects on downward SW fluxes, it is shown that as aerosol optical depth increase from 0.1 to 1.0, the relative difference increases from 0.5% to 4.4% for total and 0.8% to 4.3% for diffuse fluxes. The relatively large difference between the two models for heavy aerosol loading is mainly due to the different aerosol models used. The aerosol models included in SBDART were derived from those provided in the 5s (Tanre, 1988) and LOWTRAN7 computer codes (Shettle and Fenn, 1975), while the aerosol models in the new inference scheme were derived from OPAC (Hess et al., 1998). These aerosol models differ in aerosol constituents, vertical profiles and spectral dependence of aerosol optical properties, and thus are exerting different radiative effects on the radiation budget.

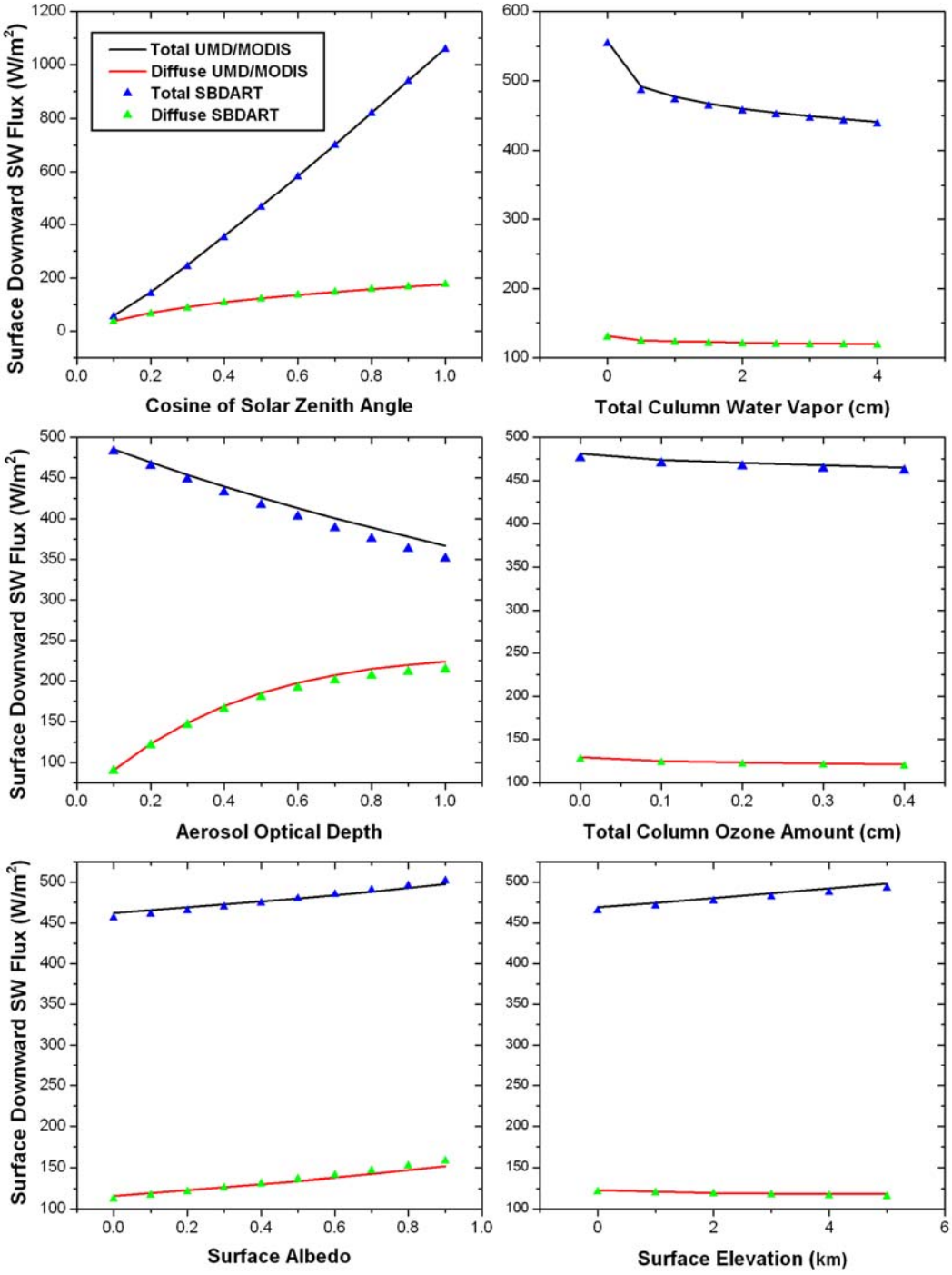

Figure 2.2 Comparison of total and diffuse SW downward flux computed from the new inference scheme and SBDART for different atmospheric and surface conditions under clear sky.

For varying surface albedo, the relative difference between the two models is small, ranging from 0.1% to 1.0% for the total flux and 0.3% to 3.6% for the diffuse part. At different surface elevations, the two models agree well with each other, having a relative difference ranging from 0.8-1.1 % for total and 0.4-2.5 % for diffuse.

2.5.2 Cloudy Sky

The cloudy sky condition used for the evaluation is specified as a cloudy mid-latitude atmosphere with: cosine of solar zenith angle=0.5, aerosol optical depth=0.2, precipitable water=0.14 cm, total zone amount=0.25 cm, surface albedo=0.2 and surface elevation =0.0 km. The liquid cloud layer is placed between 3 to 4 km, with a cloud droplet effective radius of 8 μm and a cloud optical depth of 15. The ice cloud layer is locates between 10.5 and 11 km and its cloud particle effective radius is 20 μm and optical depth is 1.

The comparison between the new inference scheme and SBDART for cloudy sky is presented in Figure 2.3. For water clouds with a r_e of 8 μm, the new inference scheme overestimates total and diffuse fluxes for optical depth less than 8 and underestimates them for optically thick clouds when compared with SBDART. The relative differences are from 0.7% to 5.7%. However, for cloud optical depth less than 16, the relative differences are around 2-3 %. It should be noted that the larger relative differences are for optically thick clouds. Though the relative value seems large, the absolute value of difference is just a few W/m^{-2}. The global mean cloud optical depth reported from ISCCP is 3.8 (Rossow et al., 1999). Thus, for most cases,

the inference scheme is in good agreement with SBDART in describing radiative effect of water clouds. For a given cloud droplet effective radius, the relative differences are around 2% for both total and diffuse fluxes.

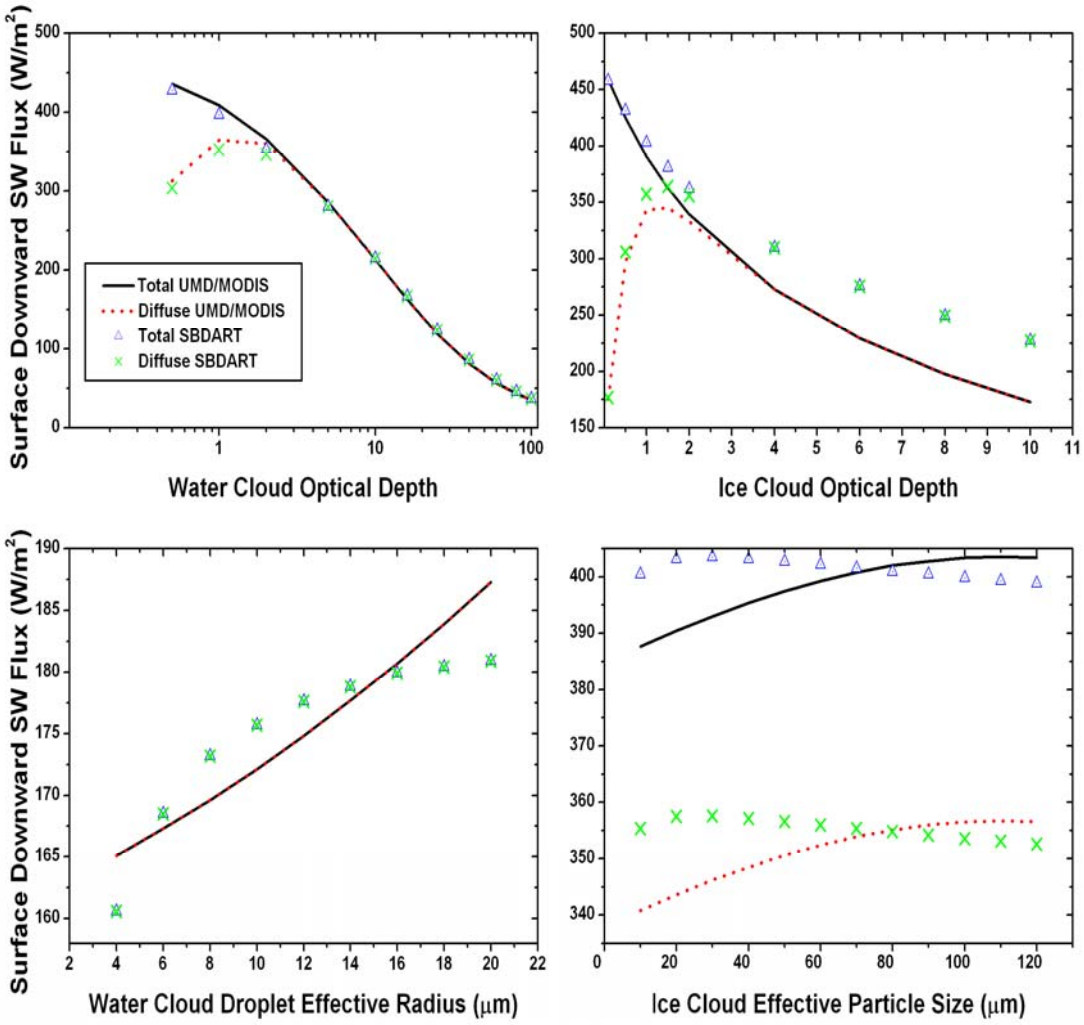

Figure 2.3 Comparison of surface downward total and diffuse SW flux computed with the new inference scheme and SBDART for water and ice clouds.

The relative differences for ice clouds are large, increasing from 0. 3% to 23.8 % as cloud optical depth increases from 0.1 to 10. Both total and diffuse fluxes computed by SBDART are larger than those from the new inference scheme. SBDART fluxes exhibit almost no variation with the change of ice crystal effective radius whereas the new results increase as ice crystal effective radius becomes larger. The large differences for ice clouds are caused by the different parameterization for ice cloud optical properties in the two models. The ice cloud radiative properties of SBDART are determined from Mie theory assuming ice crystals as spherical particles. Ice crystals may take on a variety of shapes (Takano and Liou, 1989; Schmidt et al., 1995). It has been demonstrated that the approximation of non-spherical ice crystals as equivalent ice spheres for single scattering and radiative transfer processes can substantially underestimate the solar albedo of ice clouds. The ice cloud parameterization in the new inference scheme takes into account the non-sphericity of ice crystals and particle habits type as well and thus provides a more realistic description of ice cloud optical properties than that given in SBDART.

Chapter 3: Preliminary experiments

As Terra was launched, motivated by the enhanced capabilities of the MODIS instrument for monitoring the Earth-Atmosphere System, an effort was initiated at the University of Maryland to develop inference schemes for estimating radiative fluxes that can utilize information from the new generation of satellites. The effort proceeded at several levels. Initially, the UMD/SRB model was modified (UMD/SRB_M) to bypass the need to retrieve cloud and aerosol optical properties as part of the retrieval methodology, and instead, allow the use of independent information on such parameters; the rest of the methodology remained intact. Before the availability of MODIS products, precursors of optical properties of aerosols and clouds were used to drive the model. The feasibility of such an approach as well as an assessment of the impact of using independently derived cloud properties from multi-channel retrievals on the derived radiative fluxes was investigated.

3.1 Radiative flux from AVHRR over oceans

The UMD/SRB_M version was implemented with monthly mean cloud and aerosol optical depth over oceans, derived from the AVHRR instrument by Nakajima (1995) and Higurashi (1999), respectively, for November, and December of 1996 and January of 1997, at a resolution of 0.5 degree, to estimate the surface shortwave fluxes. Cloud fraction, precipitable water, ozone amount and cosine of solar zenith angle were taken from ISCCP D1 (Rossow et al., 1996). The estimated fluxes as well as those derived from ISCCP D1 by the UMD/SRB model are illustrated in Figures 3.1 and 3.2. The comparison shows that both capture the characteristics of the global

patterns of the surface shortwave fluxes over the oceans. The discrepancies between the two may be attributed to the use of cloud fraction from ISCCP D1 and differences of spatial and temporal resolution between the AVHHR (1^0) and the ISCCP D1 products (2.5^0). The primary objective was a "proof of concept" experiment to test part of the new infra-structure of proposed model.

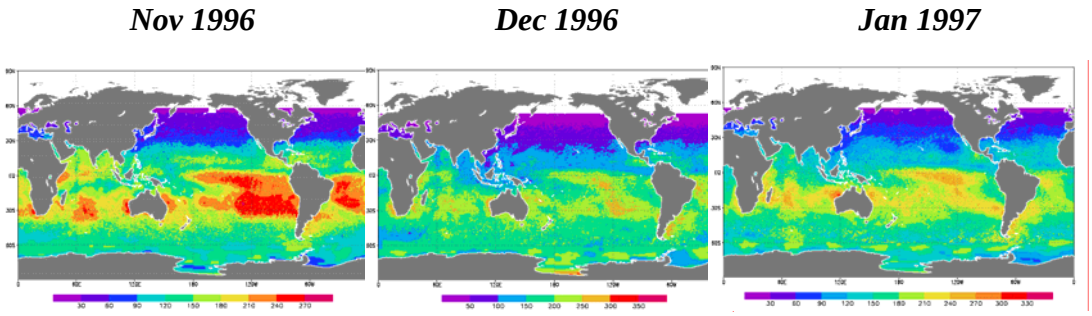

Figure 3.1 The SW surface downward flux from the UMD/SRB_M model as implemented with cloud and aerosol optical depths derived from AVHRR.

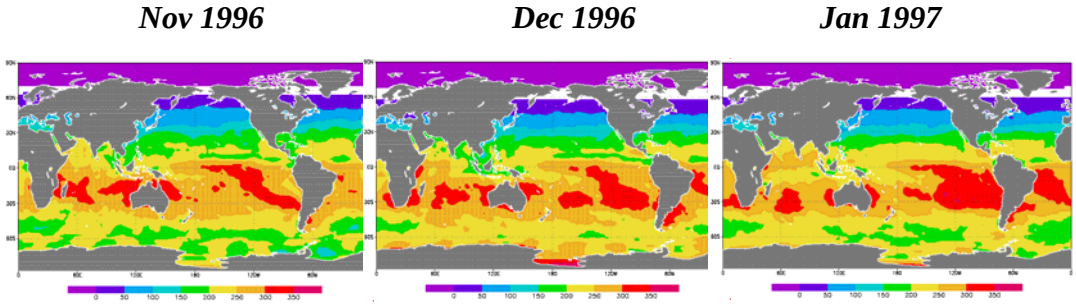

Figure 3.2 The SW surface downward flux from the UMD/SRB model implemented with ISCCP D1 data.

3.2 Impact of using independently derived cloud optical properties

In this experiment, in addition of testing the ability to implement the UMD/SRB_M version with independently derived cloud propertied, the impact of using such information on the accuracy of the radiative flux estimates was also evaluated. Specifically, the cloud properties derived by the National Aeronautics and Space Administration (NASA) Langley Cloud and Radiation Research Group over the Atmospheric Radiation Measurement (ARM) Southern Great Plains from Geostationary Operational Environmental Satellites-8 (GOES-8) (Minnis et al., 2002) are chosen for the evaluation. The retrieval of cloud properties is based on Visible-Infrared-Solar Infrared-Split (VISST) Windows method, which is an update of Solar-Solar Infrared-Infrared method described by Minnis et al. (1995). The spatial coverage of the derived cloud properties extends from 32.25^0 to 41.75^0 N and 91.25^0 to 104.750 W at 0.5-degree latitude-longitude grid. These half-hourly cloud properties for the whole period of 2000 are used to drive the model. To isolate the effect of independently derived cloud properties, all the remaining input information such as aerosol optical depth, water vapor, ozone and surface albedo are kept same as used in the original UMD/SRB model. The estimated surface shortwave fluxes are evaluated against ground observation at the Southern Great Plain of the ARM Central Facility, as well as at 4 extended ARM sites.

The derived fluxes are compared with those obtained from the UMD/SRB model as implemented for use at 0.5 degree spatial resolution over the United States in support of the GEWEX Continental Scale International Project (GCIP) and GEWEX Americas Prediction Project (GAPP) (internally known as Version 2.1) of

GCIP/GAPP UMD/SRB model (Li et al., 2007). This version is an update of Version 1.1 currently used operationally at the NOAA/National Environmental Satellite Data and Information Service (NESDIS). Specifically, it uses an updated calibration, improved cloud detection scheme over snow, and improved atmospheric input parameters such as ozone (which in Version 1.1 is taken from climatology) (Li et al., 2007; Pinker et al., 2007).

Figure 3.3 shows evaluation results against ARM central facility observations for the whole period of 2000. Over this period, the ARM SGP VISST cloud properties derived by multi-channel approach do yield better estimates of surface fluxes except for the winter months. When snow is on the ground, fluxes from Version 2.1 of the UMD/SRB model have a smaller bias than those from ARM SGP VISST cloud properties. The overall performance of the ARM SGP VISST cloud properties is indicative of possible improvement in radiative flux estimation by utilizing independently derived cloud properties based on multi-channel retrievals.

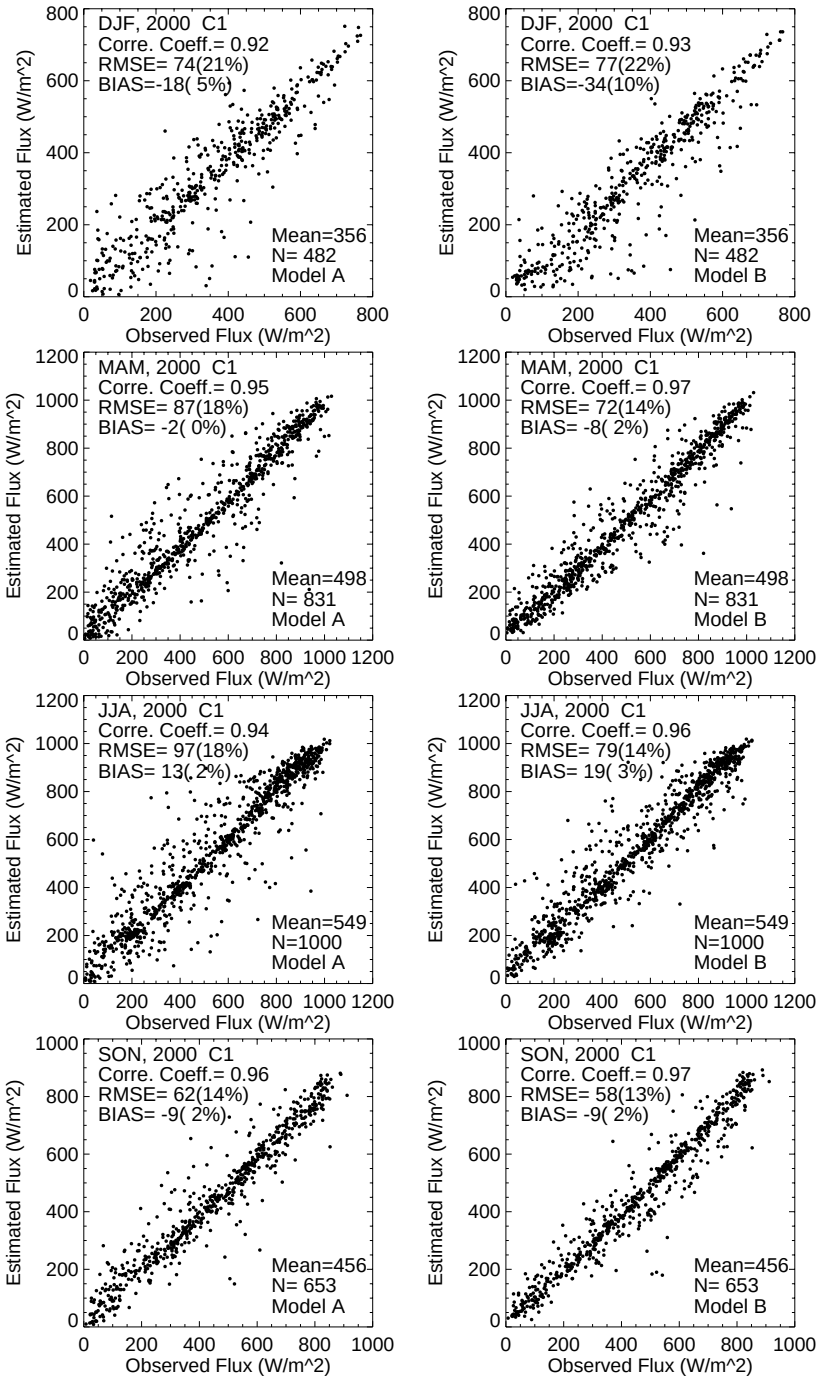

Figure 3.3 Evaluation of SW downward fluxes as estimated from the Minnis et al. (2002) cloud products using UMD/SRB_M (B) model and as derived by UMD/SRB (A) model over Central Facility SGP of ARM.

Chapter 4: Radiative fluxes based on MODIS

The new inference scheme (UMD/MODIS) was implemented with MODIS products to estimate SW radiative fluxes at different spatial scales. Specifically, MODIS Level-3 global daily product from both Terra and Aqua were used to produce fluxes at 1^0 longitude/latitude grids globally. MODIS Level-2 swath products were used to produce fluxes at 5 km resolution over North America.

4.1 Radiative fluxes based on MODIS global products

4.1.1 Input data description

Level-3 MODIS Atmosphere Daily Global Product (MOD08_D3, MYD08_D3) contains statistics derived from four Level-2 atmospheric products: aerosol (MOD04, MYD04), precipitable water (MOD05, MYD05), cloud (MOD06, MYD06), and atmospheric profiles (MOD07, MYD07), where MOD denotes data collected from Terra platform and MYD indicates data collected from Aqua platform. The statistics are sorted into 1^0 cells on an equal-angle global grid (360x180 cells).

Model input parameters taken from Level-3 Atmosphere Daily Global Product include: Optical Depth Land And Ocean, Cloud Top Pressure Day, Cloud Optical Thickness Liquid, Cloud Optical Thickness Ice, Cloud Effective Radius Liquid, Cloud Effective Radius Ice, Cloud Effective Radius Undetermined, Cloud Fraction Liquid, Cloud Fraction Ice, Cloud Fraction Undetermined, Cloud Optical Thickness Undetermined, Total Ozone, Atmospheric Water Vapor. Clouds with

undetermined phase are treated as water clouds in the computation of radiative fluxes. Level-3 Atmosphere Global Daily products from both Terra and Aqua acquired for this study are Collection 005 MODIS data from September 2002 to August 2003.

Since the MODIS atmospheric water vapor is retrieved only when at least 9 out of 25 Field of Views (FOV) are cloud free, precipitable water from the National Centers for Environmental Prediction (NCEP) Reanalysis Data (Kalnay et al., 1996) is used for conditions with large cloud fraction. Missing aerosol optical depths over arid areas are filled with information from the MODIS-Global Ozone Chemistry Aerosol Radiation Transport (GOCART) integrated monthly aerosol optical depth as provided by the school of Earth and Atmosphere Sciences, Georgia Institute of Technology (Yu et al., 2003). Spectral surface albedo at 1^0 longitude/latitude grid cell is taken from The Filled Land Surface Albedo Product, which is generated by the MODIS Atmosphere team from MOD43B3 (the official Terra/MODIS-derived Land Surface Albedo Product) (Moody el al., 2005). Monthly mean sea ice extent data at 1^0 longitude/latitude grid cells based on Special Sensor Microwave/Imager (SSM/I) are taken from NOAA/NESDIS National Climate Data Center (NCDC). Surface albedo of ice over oceans at visible and near-infrared is given as 0.77 and 0.33 respectively. The surface elevation at 1^0 longitude/latitude grid is calculated from the global Digital Elevation Model (DEM) used in the Penn State University/National Center for Atmospheric Research (PSU/NCAR) mesoscale model (known as MM5) (courtesy of Y. Ma).

4.1.2 Evaluation

The estimated surface SW downward fluxes at 10:30 and 13:30 local time are evaluated against ground measurements from 30 Baseline Surface Radiation Network (BSRN) sites (Ohmura et al., 1998). BSRN is a project of the World Climate Research Programme (WCRP) and GEWEX. Currently, there are more than 30 stations located in contrasting climatic zones, covering a latitude range from 80°N to 90°S (Figure 4.1). Solar and atmospheric radiation is measured with instruments of the highest available quality at temporal resolution of 1 to 3 minutes. In this study, 30 stations were chosen for validation (Table 4.1). As suggested by BSRN, the global incident irradiance at the surface should be computed as the sum from measured direct and diffuse radiation to lower the "cosine response error" of widely used pyranometers (Flowers and Maxwell, 1986; Ohmura et al., 1998). For the evaluation of the instantaneous fluxes, the measured irradiances were averaged over 60 minutes centered on the satellite overpass to reduce large variance caused by broken cloud fields.

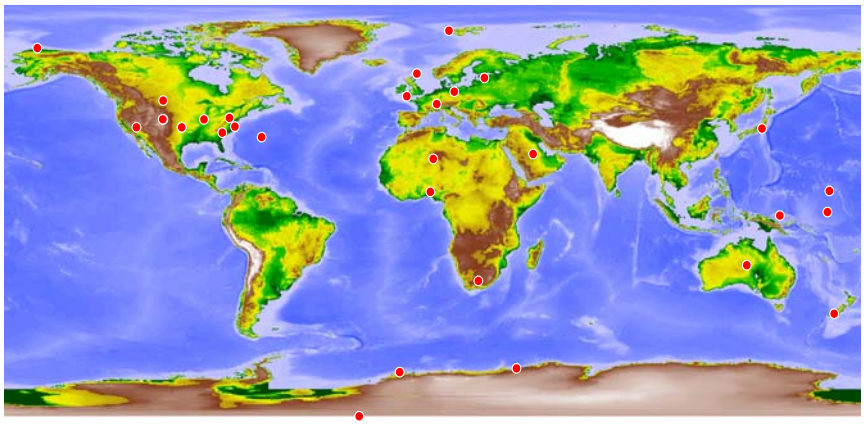

Figure 4.1 Distribution of BSRN stations

Table 4.1 BSRN sites used for evaluation

Station Name	Abbrev.	Sponsor	Latitude	Longitude
Ny Ålesund, Spitsbergen (N)	NYA	Germany/Norway	78° 56' N	11° 57' E
Barrow, Alaska	BAR	USA	71° 19' N	156° 36' W
Lerwick, Shetland Islands	LER	Great Britain	60° 08' N	1° 11' W
Toravere	TOR	Estonia	58° 16' N	26° 28' E
Lindenberg	LIN	Germany	52° 13' N	14° 07' E
Camborne	CAM	Great Britain	50° 13' N	5° 19'W
Regina	REG	Canada	50° 12' N	104° 43' W
Fort Peck, SURFRAD, CO Montana	FPE	USA	48° 19' N	105° 06' W
Payerne	PAY	Switzerland	46° 49' N	6° 57' E
Rock Springs, SURFRAD	PSU	USA	40° 43' N	77° 56' W
Boulder, SURFRAD, Co.	BOS	USA	40° 08' N	105° 14' W
Bondville, Illinois	BON	USA	40° 04' N	88° 22' W
Boulder, Colorado	BOU	USA	40° 03' N	105°00' W
Chesapeake Lt. Station	CLH	Virginia, USA	36° 54' N	75° 43' W
Desert Rock, SURFRAD, PA	DRA	USA	36° 39' N	116° 1' W
Billings, ARM/CART, OK.,	BIL	USA	36° 36' N	97° 31' W
S. Great Plains, Ext. Facil. 13, ARM	E13	USA	36° 36' N	97° 30' W
Tateno	TAT	Japan	36° 03' N	140° 08' E
Goodwin Creek, Mississippi	GCR	USA	34° 15' N	89° 52' W
Bermuda	BER	USA	32° 18' N	64° 46' W
Sede Boqer	SBO	Israel	30° 52' N	34° 46' E
Tamanrasset	TAM	Algeria	22° 47' N	5° 31' E
Kwajalein, Marshall Islands	KWA	USA	8° 43' N	167° 44' E
Ilorin	ILO	Nigeria/USA	8° 32' N	4° 34' E
Nauru Island, ARM	NAU	USA	0° 31' S	166° 55' E
Alice Springs	ASP	Australia	23° 48' S	133° 53' E
De Aar	DAA	South Africa	30° 40' S	24° 00' E
Lauder	LAU	New Zealand	45° 00' S	169° 41' E
Syowa, Antarctica	SYO	Japan	69° 00' S	39° 35' E
Georg von Neumayer, Ant.	GVN	Germany	70° 39' S	8° 15' W
South Pole, Antarctica	SPO	USA	90° S	-

The BSRN sites are classified into 7 groups: Arctic, Antarctic, Pacific islands, Atlantic Islands, North America, Europe and other continental sites. The differences between observed and estimated fluxes are summarized according to bias, root mean spare error (RMSE) and correlation coefficient. In Table 4.2 shown are results for instantaneous fluxes. Antarctic sites displayed the smallest relative bias (1%) and

relative RMSE (16%) while the largest bias (13%) and RMSE (37%) were found at Arctic sites. In general, over land, estimated fluxes agree better with ground measurement than those over ocean sites, possibly, due to the lower quality of the surface measurements over oceans.

Table 4.2 Evaluation of the Instantaneous Surface downward SW flux as derived from MODIS Global Daily Products against BSRN measurements (September 2002-August 2003)

Region	*Mean Obs Terra/Aqua*	*Cor Coef Terra/Aqua*	*RMSE (%) Terra/Aqua*	*BIAS (%) Terra/Aqua*	*# Samples Terra/Aqua*
Arctic	288/278	0.80/0.83	107(37)/97(35)	-37(13)/-22(8)	432/430
Antarctic	436/435	0.92/0.94	81(18)/72(16)	-5(1)/1(0)	436/435
Pacific	612/620	0.87/0.84	138(22)/147(24)	14(2)/13(2)	921/1018
Atlantic	449/453	0.92/0.91	110(24)/120(26)	22(5)/22(5)	989/991
North America	581/566	0.90/0.90	122(21)/122(22)	-26(5)/-25(4)	3431/3443
Europe	373/373	0.93/0.93	98(26)/99(27)	23(6)/18(5)	986/987
Other Cont sites	643/621	0.94/0.91	101(16)/124(20)	19(3)/25(4)	1916/1913

4.1.3 Daily average surface downward SW flux

Sun-synchronous satellites are restricted in their temporal coverage and obtaining reliable daily estimates of radiative fluxes from the limited number of observations remains a challenge. The diurnal variation of incident flux is caused mainly by clouds and relative position of the sun to the earth surface. While the

variation due to sun position are well described, large uncertainty still remains for depicting diurnal variation attributed to clouds. Diurnal changes of radiative fluxes between morning and afternoon are investigated using MODIS observation from both Terra and Aqua (three hours apart).

Figure 4.1 shows the difference of seasonal average surface downward SW fluxes between Terra and Aqua for September, October and November (SON); December, January and February (DJF); March, April and May (MAM); June, July and August (JJA). Positive values indicate that Terra fluxes are larger than those from Aqua whereas negative values mean the opposite. The difference between morning and afternoon fluxes displays distinctive geographic and seasonal characteristics. Over most of the continents, SW surface downward radiation is larger in the morning than in the afternoon. Large positive differences are found over Tibet Plateau, central South America, southern Africa, and the south eastern part of North America. Over much of the oceans, the differences are negative. There are consistent large negative differences over eastern south Pacific, eastern south Atlantic, eastern south Indian Ocean and eastern Pacific along the coast of California. The differences change seasonally, remain positive over land and negative over the above ocean regions, reaching maximum in local summer and abating in local winter. The diurnal variation pattern is consistent with cloud dynamics. Over the oceans at low latitudes, clouds are more common in the morning than in the afternoon while over land there are more clouds in the afternoon. The diurnal cycles of clouds over oceans are driven more by radiative cooling of the cloud tops than the surface solar insolation, which

drives the land diurnal cycles (Chen and Houze, 1997; Duvel, 1989; Gray and Jacobson, 1977). Over oceans, during daytime, absorption of solar radiation heats

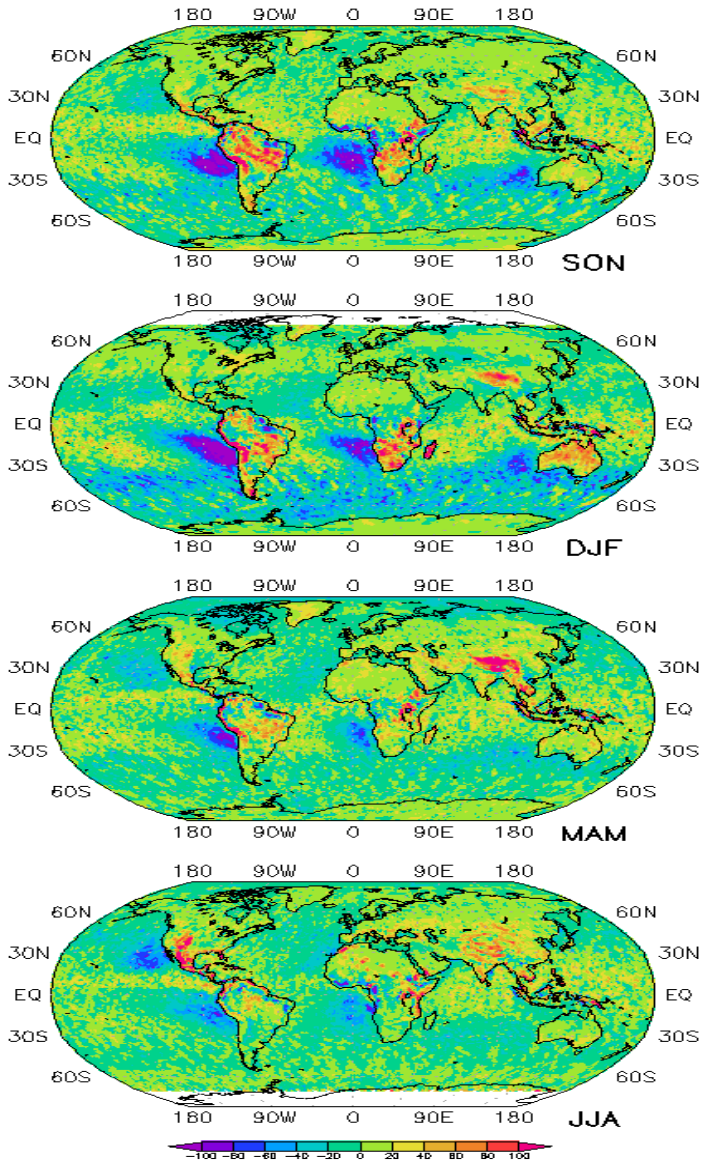

Figure 4.2 The seasonal mean difference of instantaneous surface downward SW flux between Terra at local time of 10:30 am and Aqua at local time of 13:30 pm.

the cloud tops and thus stabilizes the upper levels and inhibits the convective growth. The longwave cooling at night destabilizes cloud tops and enhances convective

growth, which reaches its maxima in early morning. Over land, the diurnal variation of radiative heating at the surface and in the lower atmosphere is larger than over oceans. The solar radiative heating drives the cloud growth which reaches its maxima in the afternoon over land.

The combination of MODIS observations from Terra and Aqua provides an opportunity to construct daily fluxes in particular due to the consistency in instrument configuration and retrieval methodologies for both satellites.

The daily average is computed by assuming that MODIS observations from Terra at 10:30 local time and from Aqua at 13:30 local time represent the atmospheric conditions from sunrise to local noon and from local noon to sunset, respectively. The diurnal variation of incident fluxes is now dictated only by the incident solar flux at top of the atmosphere which is determined by the cosine of solar zenith angle. The daily integration of radiative fluxes is reduced to the integration of the cosine of the solar zenith angle. Thus the daily mean radiative fluxes are calculated as:

$$\begin{aligned} Flux_{daily} &= \int_{Sunrise}^{Noon} Flux_{10:30} \Big/ \mu_{10:30} \, \mu(t)dt + \int_{Noon}^{Sunset} Flux_{13:30} \Big/ \mu_{10:30} \, \mu(t)dt) \\ &= Flux_{10:30} \Big/ \mu_{10:30} \, \widetilde{\mu}_{Morning} \frac{1}{2} dlen + Flux_{13:30} \Big/ \mu_{13:30} \, \widetilde{\mu}_{Afternoon} \frac{1}{2} dlen \end{aligned} \quad (4.1)$$

where $Flux_{10:30}$ and $Flux_{13:30}$ are instantaneous radiative fluxes at local 10:30 am from Terra and at local 13:30 pm from Aqua; $\mu_{10:30}$ and $\mu_{13:30}$ are cosine of solar zenith angle at local 10:30 am and 13:30 pm; and $\widetilde{\mu}_{Morning}$ and $\widetilde{\mu}_{Afternoon}$ are mean of cosine of solar zenith angle from sunrise to local noon and from local noon to sunset

respectively; dlen is the length of daytime in hours. Since cosine of solar zenith angle at local 10:30 equals cosine of solar zenith angle at local 13:30 pm and mean of cosine of solar zenith angle from sunrise to local noon equals that from local noon to sunset and is also the same as daily mean of cosine of solar zenith angle, Equation 4.1 is reduced to:

$$Flux_{daily} = \frac{1}{2}\frac{\tilde{\mu}}{\mu_{10:30}} dlen\left(Flux_{10:30} + Flux_{13:30}\right)/24 \quad (4.2)$$

where ũ is the daily mean of cosine of solar zenith angle.

4.1.4 Evaluation

The satellite based estimates of the daily average surface downward SW flux are evaluated by comparison with BSRN ground observations. The evaluation process follows the procedures used for instantaneous fluxes. Results are summarized in Table 4.3. When compared to instantaneous fluxes, results improve greatly. Except for the Arctic zone and the tropical western Pacific, the correlation coefficient is greater than 0.95, the relative RMSE is less than 20%, and relative bias is from 0 to 2%. For Arctic sites, the correlation coefficient improves from 0.80 for instantaneous fluxes to 0.92 for daily averages. However, a relative RMSE of 27% and a relative bias of 10% are still relatively large. The negative bias for both instantaneous and daily averaged fluxes implies that the underestimate of the surface downward SW fluxes is systematic. This might be due to the still existing problems to identify clouds over very bright surfaces. The sites in the Pacific display the lowest relative correlation coefficient (0.80). Two of the three sites are located in the tropical western Pacific, often known as the “warm pool” region and frequented by deep

convection and strong diurnal variation in clouds. Possibly, two MODIS observations are not sufficient to represent the diurnal variation of radiative fluxes.

Table 4.3 Evaluation of daily average surface downward SW flux (W/m^2) derived from MODIS against BSRN measurements (September 2002-August 2003)

Region	Mean obser	Cor .Coef.	RMSE (%)	BIAS (%)	# Obser
Arctic	138	0.92	37 (27)	-14 (10)	426
Antarctic	230	0.97	31 (14)	-5 (2)	578
Pacific	202	0.80	51 (25)	-1 (1)	1041
Atlantic	154	0.96	29 (19)	0 (0)	995
North Am	179	0.96	31 (18)	-12 (7)	2869
Europe	128	0.97	25 (19)	2 (1)	984
Other Cont	214	0.95	31 (14)	-1 (0)	1934

4.1.5 Comparison with independent satellites

Three datasets have been selected for comparison with independent satellite estimates of radiative fluxes. Two are based on ISCCP observations at 2.5^0 longitude/latitude resolution. The third one is from Clouds and the Earth's Radiant Energy System (CERES) Monthly TOA/Surface Averages (SRBAVG) product at 1^0 longitude/latitude resolution, all for the period of September 2002 to August 2003.

One set of ISCCP based estimates was derived with an updated version of the UMD/SRB model (Ma and Pinker, 2007). This version of the model accounts for elevation effects and uses updated information on aerosols (Liu et al., 2005; Liu et al., 2007). The other ISCCP product is based on the NASA Goddard Institute for Space Studies (GISS) radiative transfer model (Zhang et al., 1995; Zhang et al., 2004;

Hansen et al., 1983). The shortwave radiative fluxes are computed from cloud properties derived initially from the TOA radiances in two spectral intervals.

The CERES (Wielicki et al., 1996) dataset is based on broadband SW radiances at TOA measured by CERES spaceborne radiometer. The SW radiative fluxes at the surface are derived using the Langley Parameterized Shortwave Algorithm (LPSA) (Darnell et al. 1992; Gupta et al. 2001). This algorithm uses simplified radiative transfer parameterization to relate TOA reflected radiance to surface radiative flux.

Global annual mean solar radiation reflected to space, absorbed in the atmosphere and absorbed at surface and their percentage of the incident solar radiation at TOA from UMD/MODIS and three other datasets are presented in Table 4.4. UMD/MODIS flux is within a few percent of the other estimates. Planetary albedo from UMD/MODIS (32.2%) is larger than the ones from the other three datasets. UMD/MODIS atmospheric absorption (21.4%) is close to all three datasets. Net SW flux at the surface from UMD/MODIS (46.4%) is smaller than from both CERES and the other ISCCP estimates.

The global mean values for clear sky condition (Table 4.5) indicate that the differences in absorption in the atmosphere and at the surface between UMD/MODIS and the other datasets are comparable to those for all sky conditions. The reflected fluxes at TOA are in better agreement among the four datasets than those for all sky conditions. Figure 4.3 shows the zonal mean surface downward SW flux for January and July of 2003 and the annual mean from UMD/MODIS, CERES and the two

ISCCP datasets. UMD/MODIS values display the same latitudinal variation as the other two but are lower especially in the mid-high latitude storm track and the ITCZ that is cloudier than in the other regions. Zonal mean reflected flux is shown in Figure 4.4. It is evident that UMD/MODIS values are higher than those from the other three datasets. This implies that clouds observed by MODIS are either more frequent or thicker than those from ISCCP and CERES. The comparison of cloud properties between the four datasets is discussed in the cloud radiative forcing section.

Table 4.4 Global annual mean SW radiative flux for all sky condition from four datasets

Sources	ISCCP/GISS	ISCCP/UMD/SRB	CERES	UMD/MODIS
Reflected/space	105.2(30.8)	98.6(28.9)	96.9(28.3)	110.2(32.2)
Absorbed/atmos.	70.9(20.7)	69.4(20.2)	69.8(20.4)	71.8.0(21.4)
Absorbed/surface	165.9(48.5)	174(50.9)	175.3(51.3)	160(46.4)

Table 4.5 Global annual mean SW radiative flux for clear sky condition from four satellite based datasets

Sources	ISCCP/GISS	ISCCP/UMD/SRB	CERES	UMD/MODIS
Reflected/space	54.4 (15.9)	53.6 (15.8)	50.8(14.9)	55.4 (16.2)
Absorbed/atmos.	67.6 (19.8)	65.2 (19.2)	72.0 (21)	74.4 (21.8)
Absorbed/surface	220 (64.3)	220.5 (65.0)	219.2(64.1)	212.2 (62)

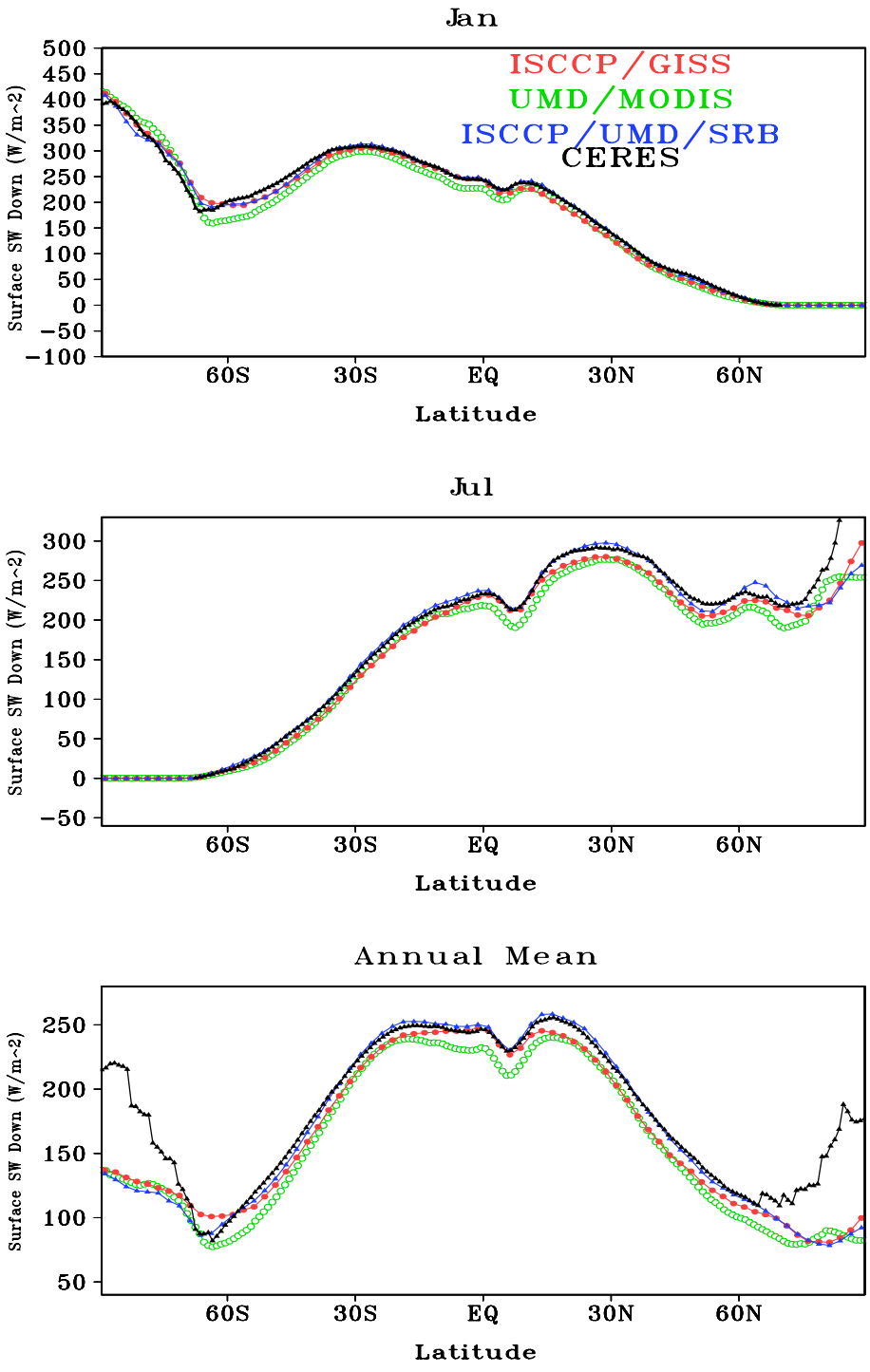

Figure 4.3 Zonal mean surface downward SW flux for 2003 from UMD/MODIS, ISCCP/GISS, ISCCP/UMD/SRB and CERES products

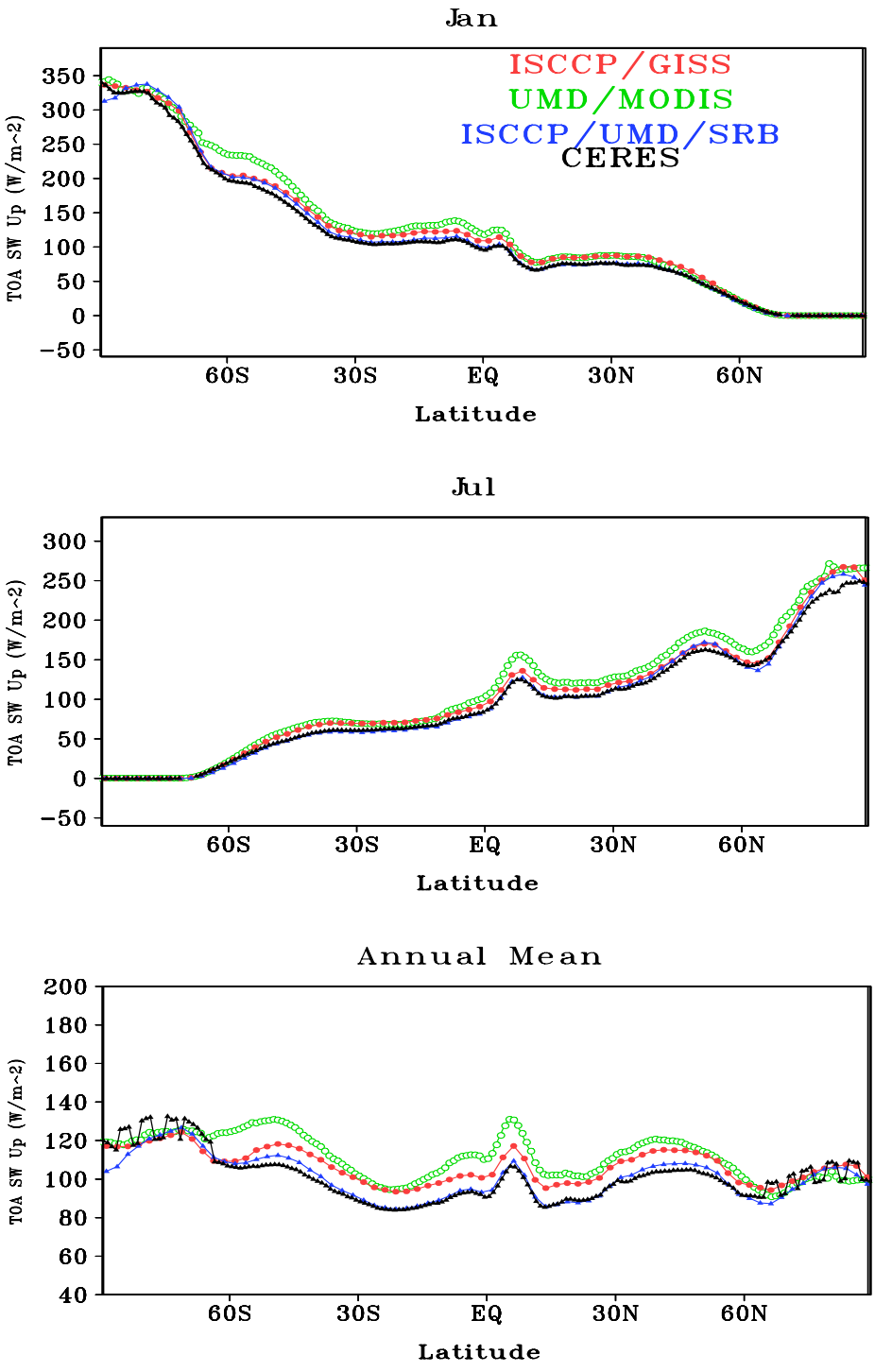

Figure 4.4 Monthly and annual zonal mean TOA upward SW flux for 2003 as available from UMD/MODIS, ISCCP/GISS, ISCCP/UMD/SRB and CERES products

To understand the differences among the estimates from the four satellite datasets, monthly mean surface downward SW fluxes are evaluated against ground measurements from 30 BSRN stations. The evaluation was done by comparing the ground measurements at every station with satellites estimates for the grid cell containing that ground station. It should be noted that UMD/MODIS and CERES estimates are at 1^0 resolution while ISCCP/GISS and ISCCP/UMD/SRB estimates were produced at 2.5^0.

Table 4.6 Comparison of monthly mean surface downward SW fluxes from UMD/MODIS, CERS, ISCCP/GISS and ISCCP/UMD/SRB against ground measurements at 30 BSRN stations. The mean of observations is 180.9 W/m^2 and there are 326 samples. (September 2002-August 2003)

Sources(Resolution)	**Cor Coef.**	**RMSE (%)**	**BIAS (%)**
UMD/MODIS(1^0)	0.98	16.1 (9)	-5.4 (3)
CERES(1^0)	0.96	24.1 (13)	-0.2 (0)
ISCCP/GISS(2.5^0)	0.96	25.0 (14)	5.6 (3)
ISCCP/UMD/SRB(2.5^0)	0.98	19.1 (11)	-3.7 (2)

Table 4.6 displays the comparison statistics for the four datasets. Compared to CERES, UMD/MODIS underestimates surface downward SW fluxes, with a larger bias of -5.4 W/m^2, a smaller RMSE of 16.1 W/m^2 and a higher correlation coefficient of 0.98. ISCCP/GISS and ISCCP/UMD/SRB estimates have similar bias to that of UMD/MODIS but have a higher RMSE of 25.0 and 19.1 W/m^2 respectively.

4.1.6 Cloud radiative forcing (CRF)

The effect of clouds on the radiation budget is usually quantified by the concept of "cloud radiative forcing", as proposed by Ramanathan et al. (1989). It is the difference between the all sky radiative flux and the clear sky radiative flux, given as:

$$CRF = F_{all} - F_{clear}, \quad (4.3)$$

where F_{all} and F_{clear} are all sky net flux and clear sky net flux respectively, defined as:

$$F_{all} = F_{all}^{-} - F_{all}^{+}, \quad (4.4)$$

$$F_{clear} = F_{clear}^{-} - F_{clear}^{+}, \quad (4.5)$$

where subscript "-" and "+" denote downward and upward flux respectively. Since clouds generally reflect more incident solar radiation than the clear sky, the SW cloud radiative forcing is positive at TOA and negative at the surface. MODIS instruments onboard Terra and Aqua, with their enhanced capabilities to detect clouds, provide an opportunity to better estimate the magnitude of cloud radiative forcing.

Monthly and annual SW cloud radative forcing at the TOA and at the surface is computed from the daily average flux at 1^0 longitude/latitude resolution. In Figure 4.4 displayed are the monthly mean values for January and July as well as the annual mean at TOA. In January, large cloud radiative forcing is present over the storm track in mid-high latitude southern hemisphere and to the south of the Amazon in South America. Values can reach up to 200 W/m^2. The Inter-Tropical Convection Zone also displays strong SW cloud radiative forcing. Low values of cloud forcing are found in equatorial and subtropical subsidence regions and in the Antarctic Continent where

clouds are less frequent. In July, as the sun moves to the northern hemisphere, strong SW cloud radiative forcing is found in ITCZ, northern Pacific and Atlantic oceans and in the Asian monsoon regions. Low cloud radiative forcing is seen over much of the subtropical regions in southern hemisphere, northern Africa, Arabian Peninsula and Greenland. The geographic distribution of cloud radiative forcing is dictated by the general circulation of atmosphere. Latitudinal variation of cloud radiative forcing as shown by zonal mean values (Figure 4.5) corresponds well to climatic zones with

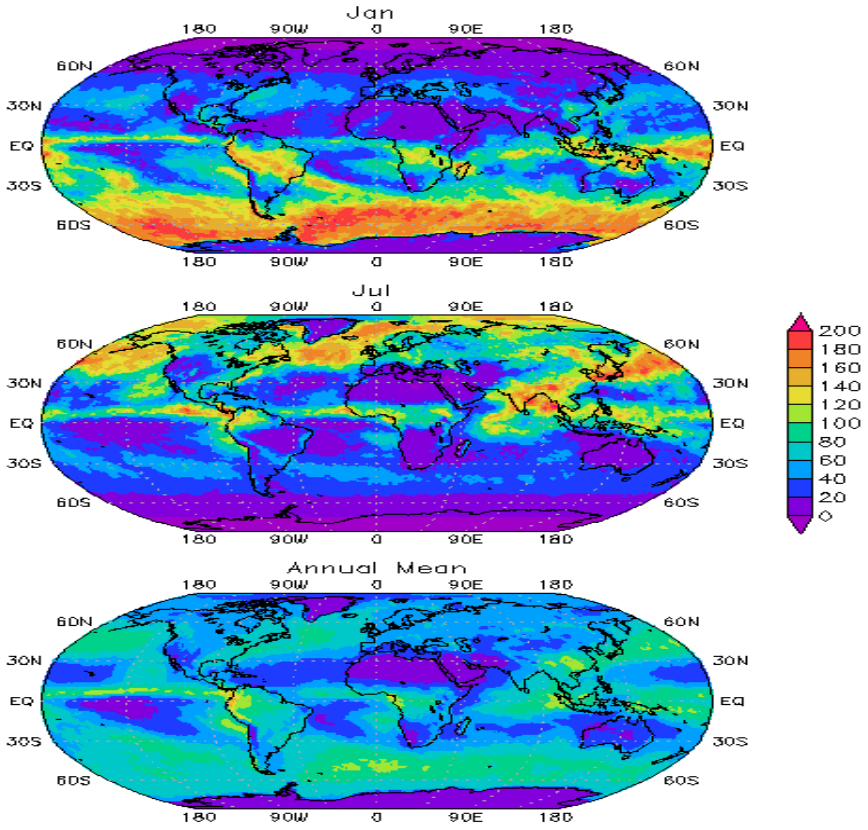

Figure 4.5 Monthly and annual mean SW cloud radiative forcing at TOA for 2003 from the UMD/MODIS product

peaks in ITCZ and mid-high latitude storm track and valleys in subtropical subsidence regions. Figure 4.6 presents the zonal mean TOA SW radiative forcing

derived for the same period from UMD/MODIS, ISCCP/GISS and CERES. The three datasets follow each other very well yet cloud radiative forcing from UMD/MODIS is larger than ISCCP/GISS and CERES. SW cloud radiative forcing at the surface is very close to that of TOA but with opposite sign. The geographic distribution of cloud radiative forcing at the surface and the TOA is essentially the same.

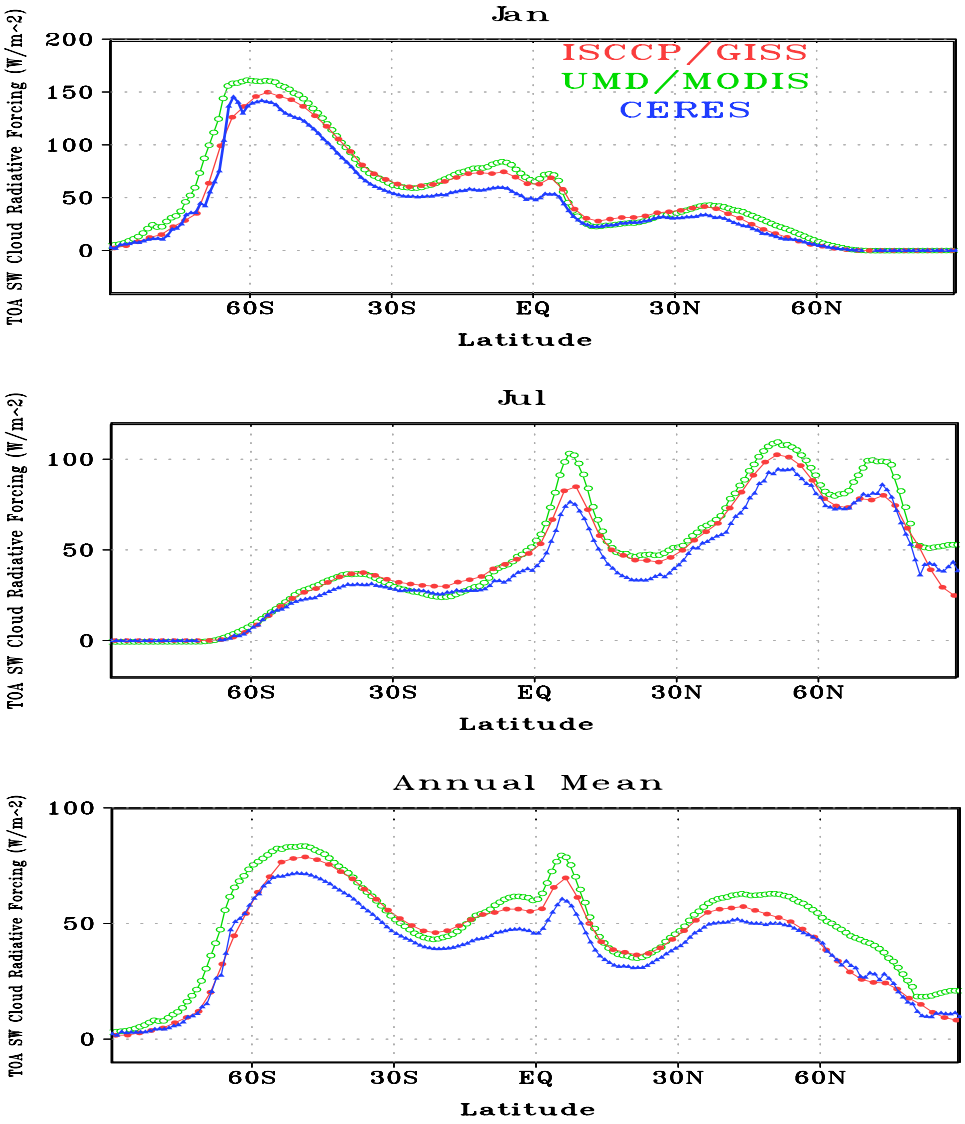

Figure 4.6 Zonal mean SW cloud radiative forcing TOA for 2003 derived from UMD/MODIS, ISCCP/GISS and CERES data

In Figures 4.7 and 4.8 shown are zonal mean cloud fraction and cloud optical depth for January and July of 2003 as well as the annual mean values for MODIS, CERES and ISCCP, respectively. Cloud fraction from MODIS is lower than that of CERES and ISCCP except for the Southern Hemisphere storm track. Differences in cloud amount between MODIS and the other two datasets can be up to 20 % in subtropical regions for both monthly and annual mean values. MOIDIS cloud optical depth is much larger than that of CERES and ISCCP in most regions. During local summer at high latitudes, CERES and ISCCP cloud optical depth is larger than that estimated from MODIS. The difference in cloud optical depth between MODIS and the other two datasets can be up to more than 10 in the mid-high latitude region. In general, clouds observed by MODIS are less frequent but much thicker than seen in CERES and ISCCP. The low cloud fraction and high cloud optical depth from MODIS relative to CERES and ISCCP have opposite effects on the radiative fluxes. In subtropical region, the two effects seem to cancel out and the SW cloud radiative forcing derived from MODIS is close to that from the other two datasets. In the mid-high latitude region and the ITCZ, the difference in cloud fraction is smaller as compared to the other regions, while the difference in cloud optical depth is large, resulting in larger cloud radiative forcing than from CERES and ISCCP.

It should be noted that there are two sources of cloud fraction information in MODIS Level-3 gridded product (Platnick et al., 2003). One is the count of cloudy and probably cloudy outcomes observed during the processing of cloud-top algorithm. It provides a cloud mask fraction calculation of the two highest confidence

cloudy bits in the mask. Another source is based on optical/microphysical retrievals. The cloud fractions of water, ice and undetermined phase clouds are provided. These are number of successful optical/microphysical retrievals normalized by the total number of clear and cloudy pixels. However, pixels associated with a failed retrieval outcome during processing are not counted in the normalization. Therefore, this cloud fraction is not necessarily the same as the former one. It is the latter one that was used in the computation of radiative fluxes and cloud forcing. Since the pixels associated with a failed retrieval outcome tend to be partially cloudy pixels or have small optical depth, excluding these pixels would most likely give rise to low cloud fraction and high cloud optical depth for a grid cell. In computing radiative fluxes, low cloud fraction and high cloud optical depth might not yield the same results as high cloud fraction and low cloud optical depth. The impact of using this cloud fraction on the accuracy of radiative fluxes needs to be examined in the future.

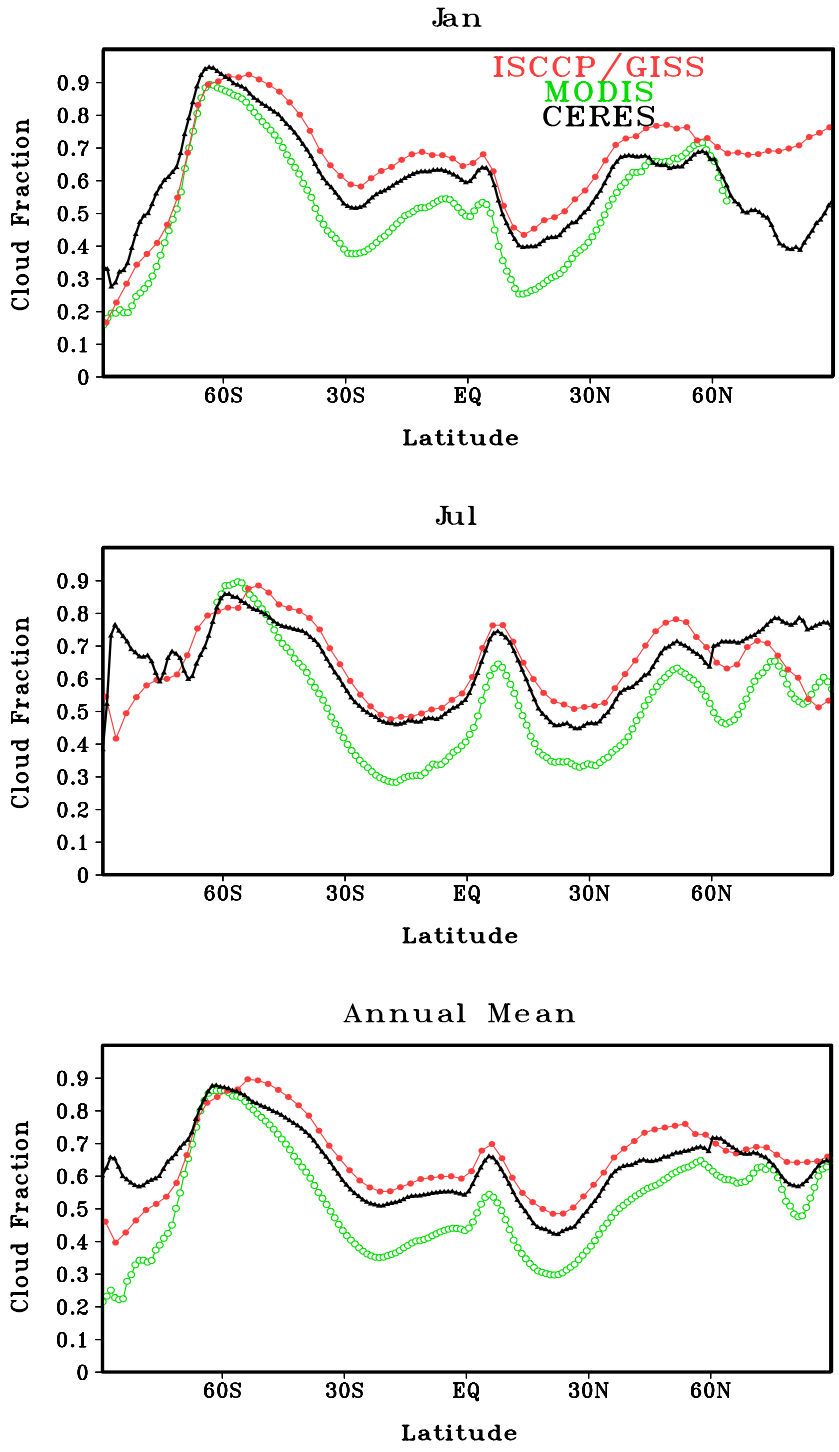

Figure 4.7 Zonal mean cloud fraction as observed by MOIDIS, CERES and ISCCP D1 (September 2002-August 2003)

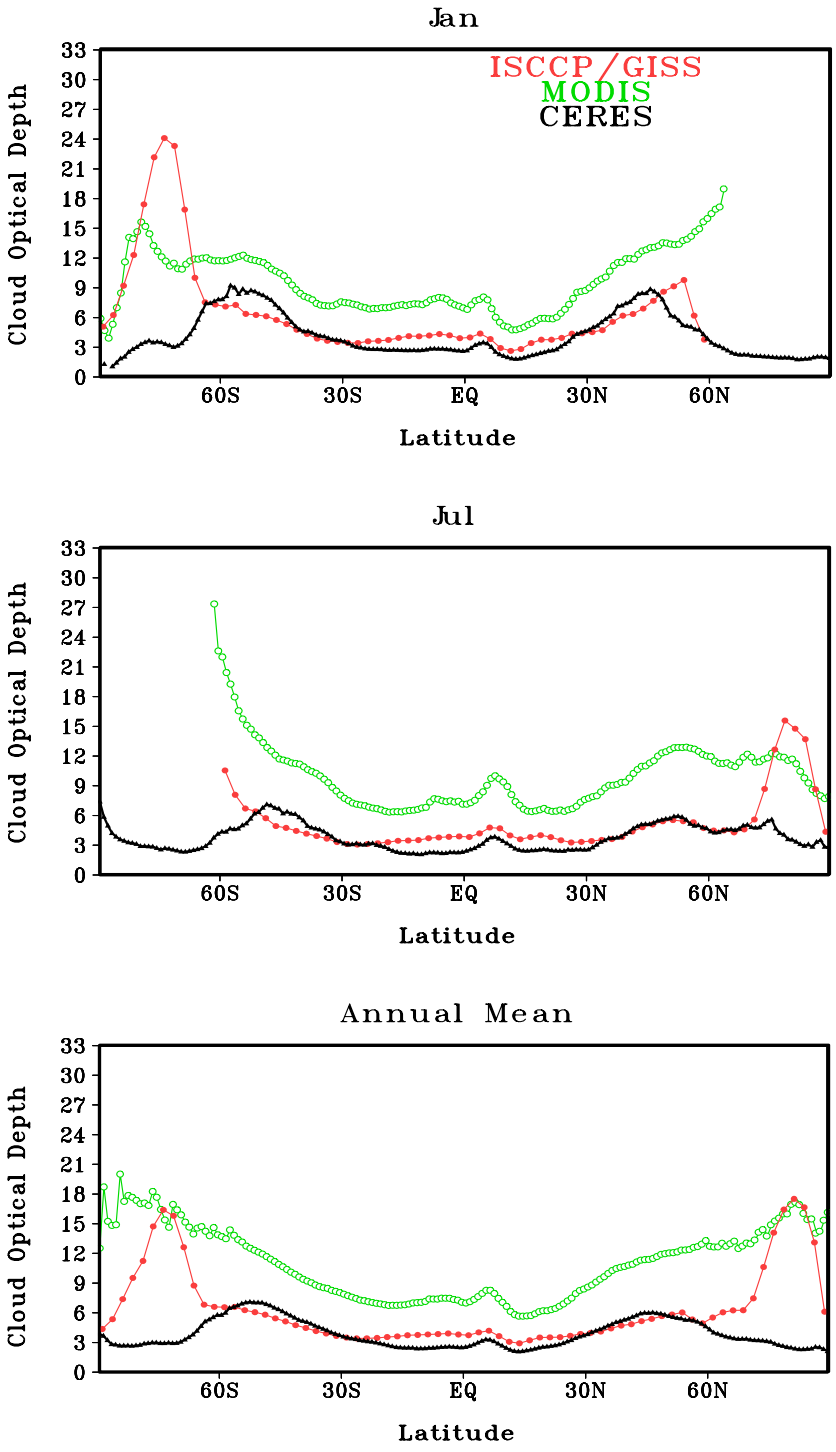

Figure 4.8 Zonal mean cloud optical depth as observed by MODIS, CERES and ISCCP D1 (September 2002-August 2003)

4.1.7 Vertical profile of SW radiative flux

Vertical profile of radiative flux determines the radiative heating in the atmosphere. This in turn has a central role in influencing the atmospheric temperature structure and affects the atmospheric circulation and cloud evolution. While GCMs can characterize the vertical profile of SW fluxes, observations of vertical profiles of radiative fluxes are almost non-existent especially under cloudy conditions. Information on the vertical profile of radiative fluxes is needed to investigate the role of radiation in hydrological and meteorological processes, to determine the forcing of clouds, aerosols, surface albedo, and to validate GCMs.

The UMD/MODIS model possesses the capability to compute vertical profiles of SW radiative fluxes, given the vertical distribution of absorbing gases and clouds. The cloud base is estimated from a statistical model which gives cloud layer thickness as a function of cloud top height, latitude, month of the year, for land and ocean separately (Wang, et al., 2000). Figure 4.9 shows the monthly mean of pressure-latitude cross section of clear and cloudy sky net SW fluxes for July of 2003 derived by UMD/MODIS model. The nearly vertical contour indicates the relative transparency of the atmosphere whereas the deviation of the contour from vertical indicates the strong water vapor absorption. It is clear that most of the SW flux is absorbed in the lower layer of the atmosphere where water vapor is abundant. The clear sky profile shows the apparent polarward decrease of net SW flux. Clouds reduce the absorbed SW fluxes and disturb the vertical profile dramatically.

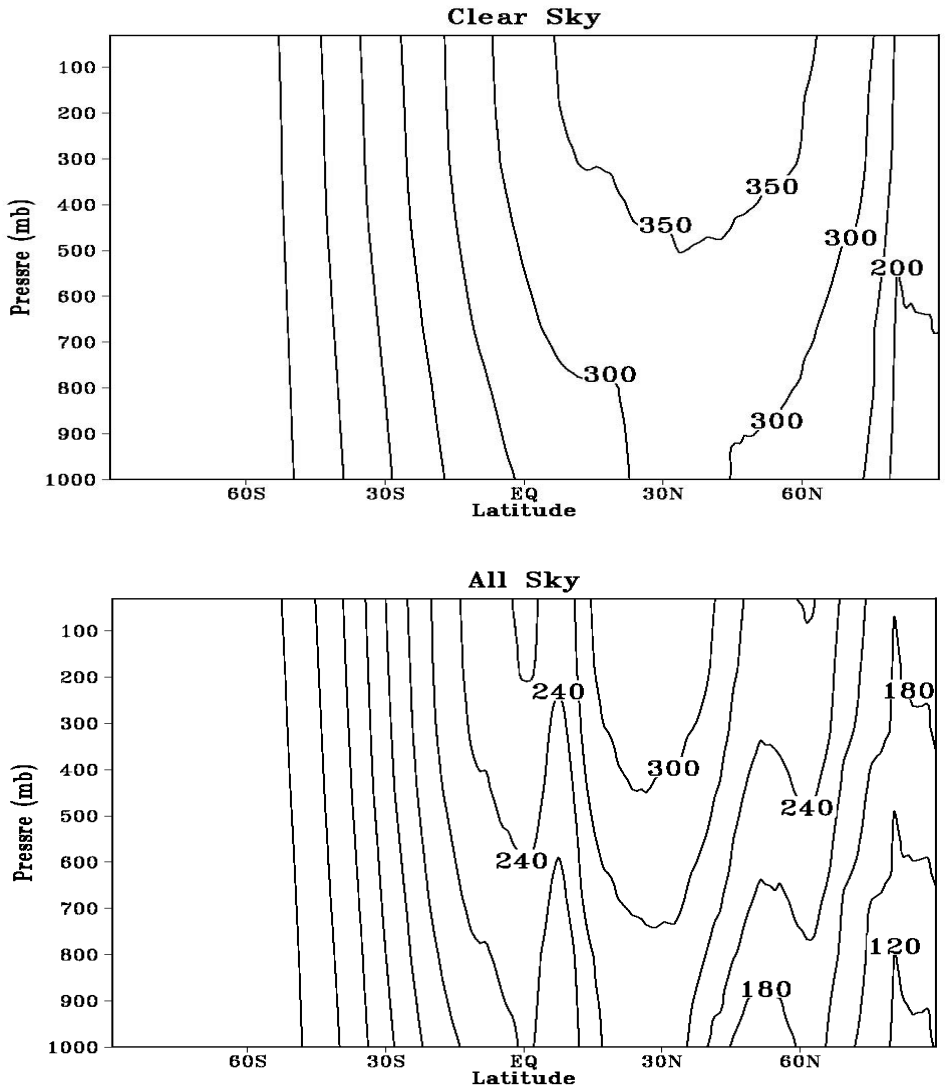

Figure 4.9 Monthly mean pressure-latitude cross section of net SW fluxes under clear and all sky conditions for July of 2003

While the lack of information on the vertical distribution of clouds limits the accuracy of vertical profiles of net SW fluxes, the use of the statistical cloud layer thickness model allows for building capabilities for future improvements. It is anticipated that with the forthcoming information on cloud vertical distribution from new generation of satellites such as CloudSat and CALIPSO it would be possible to

use the UMD/MODIS model so that a better understanding of the vertical distribution of SW fluxes can be gained.

4.1.8 SW radiative fluxes over polar regions

Recent studies have shown that the Arctic sea ice is melting three times faster than many scientists projected (Stroeve et al., 2007). The snow ice-albedo feedback is one of the major factors accelerating the melting in response to global warming (Holland and Bitz, 2003). Sea ice and snow have high albedos. With higher polar temperatures, the area of the sea ice and snow cover decreases, exposing new expanses of ocean and land surfaces to absorb an increased amount of solar radiation. This increase of total absorbed solar radiation contributes to continued and accelerated warming (Curry et al. 1995). Accurate information of SW radiative fluxes is needed in studying snow/ice albedo feedback and in assessing its impact on climate, ocean circulation and ecosystems. The SW radiative fluxes over the polar regions have been monitored primarily by satellites. Yet, estimation of radiative fluxes in the polar regions from satellites remains challenging due to the difficulty of detecting clouds over snow and ice surfaces (Li and Leighton 1991). MODIS with specific bands designed to detect clouds over snow and ice, is expected to provide better cloud detection and help to improve accuracy of radiative flux estimate over polar regions.

To assess the accuracy of MODIS SW products over the Arctic and Antarctica, monthly mean surface downward SW fluxes from UMD/MODIS, CERES, ISCCP/GISS and ISCCP/UMD/SRB are evaluated against BSRN ground

measurements. Table 4.7 presents results from four datasets over Antarctica for September 2002 to August 2003. UMD/MODIS fluxes agree extremely well with ground measurements, having a bias of -1.4 W/m^2, a RMSE of 25.7 W/m^2 and high correlation coefficient of 0.99. CERES and ISCCP/GISS underestimate the SW fluxes by 20% and 17% respectively. CERES fluxes differ the most with the ground observations, with a RMSE of 60 W/m^2.

Table 4.7 Comparison of monthly mean surface downward SW fluxes from UMD/MODIS, CERS, ISCCP/GISS and ISCCP/UMD/SRB against ground measurements at 3 BSRN stations in Antarctic. The mean of observations is 210 W/m^2 and there are 22 samples. (September 2002-August)

Sources (Resolution)	Cor .Coef.	RMSE (%)	BIAS (%)
UMD/MODIS (1^0)	0.99	25.7 (12)	-1.4 (1)
CERES (1^0)	0.95	59.8 (29)	-42.3 (20)
ISCCP/GISS (2.5^0)	0.94	56.7 (27)	-36.0 (17)
ISCCP/UMD/SRB (2.5^0)	0.97	37.2 (18)	-19.0 (9)

Table 4.8 Comparison of monthly mean surface downward SW fluxes from UMD/MODIS, CERS, ISCCP/GISS and ISCCP/UMD/SRB against ground measurements at 2 BSRN stations in Arctic. The mean of observations is 131.7 W/m^2 and there are 15 samples. (September 2002-August)

Sources (Resolution)	Cor .Coef.	RMSE (%)	BIAS (%)
UMD/MODIS (1^0)	0.97	21.9 (17)	-12.2 (9)
CERES (1^0)	0.97	24.0 (18)	11.4 (9)
ISCCP/GISS (2.5^0)	0.96	24.5 (19)	-1.0 (0)
ISCCP/UMD/SRB (2.5^0)	0.94	26.8 (20)	4.5 (3)

Over the Arctic (Table 4.8), ISCCP/GISS fluxes have the smallest bias of -1.0 W/m^2. UMD/MODIS values underestimate the surface downward SW flux by 9% while CERES overestimates it by 9%. UMD/MODIS fluxes still have the lowest RMSE (20.9 W/m^2).

4.1.9 SW radiative fluxes over the Tibet Plateau

The Tibet Plateau, with an area of 2.5 million square kilometers and average surface elevation of over 4500 meters (Figure 4.10), is the most prominent and complex terrain on the globe. It plays a very important role in the Asian monsoon system and thus exerts a large influence on the global atmospheric circulation. For advancing the understanding of the water and energy cycle over the Tibet Plateau,

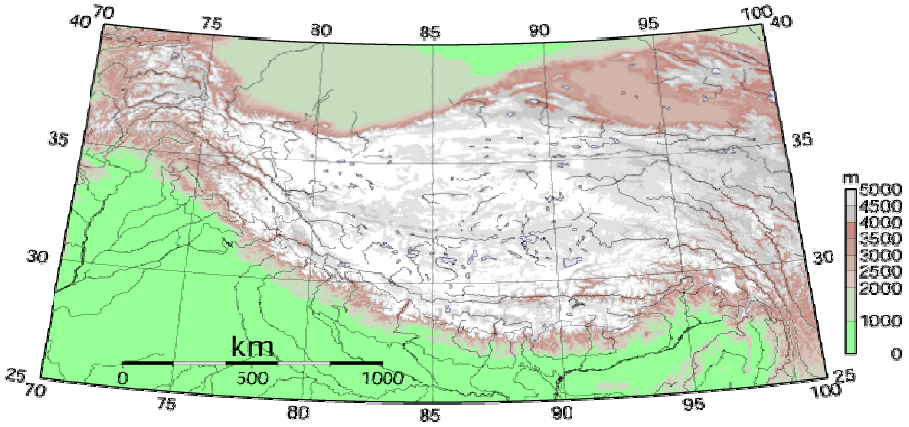

Figure 4.10 Surface elevation map of the Tibet Plateau

accurate information on surface radiation budget is needed. The very few sparsely distributed ground stations are far from sufficient to construct a detailed radiation budget. MODIS provides consistent coverage over the Plateau. Due to the high elevation, it is important to use inference schemes that can account for topographic effects. The observed surface downward shortwave fluxes at altitude of 4800 m on

the Tibet Plateau, at local noon on clear summer days are 10-15 % greater than those observed at a typical sea level station (Tanaka *et al*., 2001). Therefore, the capability of the new inference scheme to accounts for elevation effects is critical for this region.

The daily average surface downward SW flux derived by the UMD/MODIS model at 1^0 spatial resolution is compared with ground measurement at the Tibet Plateau. The ground observations are from CEOP Asia-Australia monsoon project (CAMP) on the Tibet Plateau (CAMP/Tibet, 2001-2005). Surface downward SW fluxes from six Automatic Weather Station (AWS) and two Planetary Boundary Layer (PLB) towers are used for the time period when MODIS values are available. The geo-locations and surface elevation of the eight sites are shown in Table 4.9. Evaluation results are shown in Table 4.10. The correlation coefficient between the satellite estimates and the ground observations ranges from 0.81 to 0.92. The relative RMSE is from 16 to 23%. The mean bias is low except for three sites with relatively large bias of up to 15%. Overall, there is no tendency to underestimate ground measurements. The relatively low correlation coefficient is likely due to the large spatial variability of the radiation field on the Tibet Plateau and the difficulty to capture this variability with a single ground station. As shown in Figure 4.11, D110-AWS and AMDO-Tower collocated in one grid cell box at which radiative flux is derived, and ANNI-AWS, MS3478-AWS and MS3608-AWS fall into another cell box. By averaging these sites a better representation of a single satellite grid can be achieved. Daily average values at the two sets of stations were averaged and then compared to the satellite grid value. The scatter plot of ground averaged values and

Table 4.9 CAMP sites on the Tibet Plateau

Station	Longitude	Latitude	Elevation (m)
ANNI-AWS	31.2544	92.1714	4480
AMDO-Tower	32.2410	91.6249	4695
BJ-Tower	31.3687	91.8987	4509
D105-AWS	33.0643	91.9426	5039
D110-AWS	32.6930	91.8741	4985
D66-AWS	35.5235	93.7845	4585
MS3478-AWS	31.9262	91.7147	4620
MS3608-AWS	31.2262	91.7833	4598

Table 4.10 Evaluation of daily average surface downward SW flux at CAMP sites on the Tibet Plateau (September 2002-August 2003) (W/m^2)

Station	Mean Obs	Cor Coef	Bias (%)	RMSE (%)	# Obser
ANNI-AWS	209	0.85	-1 (0)	37 (18)	334
AMDO-Tower	206	0.87	4 (2)	33 (16)	233
BJ-Tower	219	0.87	-4 (2)	35 (16)	334
D105-AWS	204	0.81	9 (4)	45 (22)	334
D110-AWS	228	0.84	-5 (2)	39 (17)	334
D66-AWS	190	0.92	28 (15)	43 (23)	334
MS3478-AWS	240	0.83	-25 (10)	47 (20)	334
MS3608-AWS	200	0.82	16 (7)	43 (21)	334

satellite estimates is presented in Figure 4.12. The agreement between measured and derived data has now greatly improved. For instance, for D110-AWS and AMDO-Tower, the correlation coefficient increased from 0.87 and 0.84 to 0.92 and the relative RMSE is reduces from 16% and 22% to 13%. The other three sites also exhibit improvement. The bias was reduced to 2%, indicating the need for better

ground representation of spatial variability or satellite estimates at higher spatial resolution.

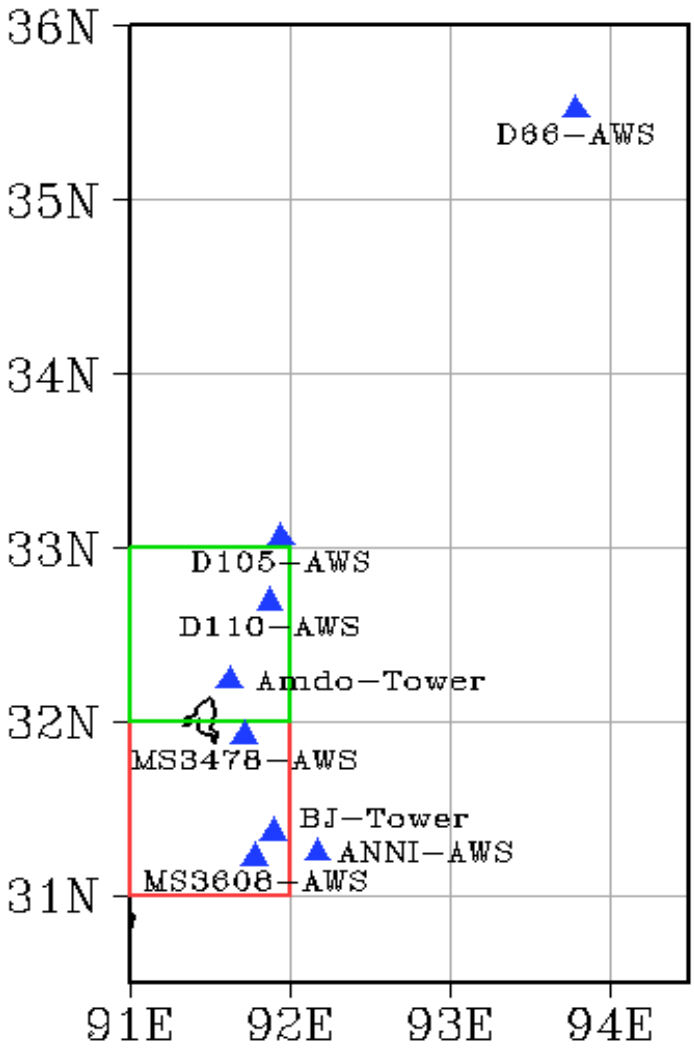

Figure 4.11 Locations of CAMP sites in grid cells for which radiative fluxes are derived from MODIS.

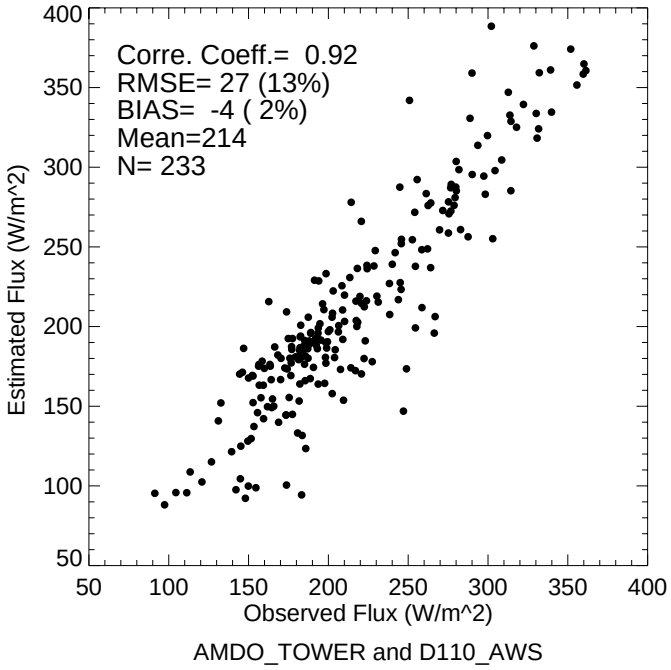

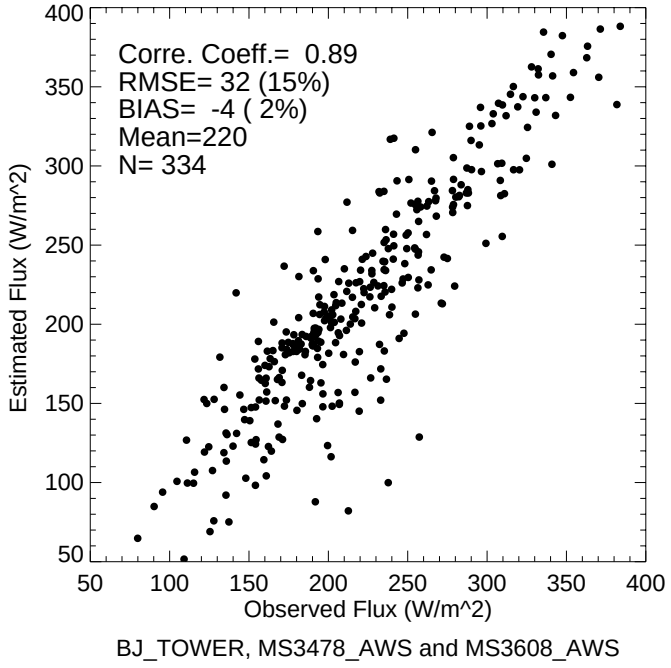

Figure 4.12 Evaluation of derived SW surface downward fluxes from UMD/MODIS model against ground measurements averaged for all sites in one grid box (September 2002-August 2003).

Most satellite datasets have difficulties in deriving surface downward SW fluxes over the Tibet Plateau due to its high elevation and complex terrain. Monthly mean surface downward SW fluxes from four datasets are compared with CAMP ground observation over the time period of September 2002 to August 2003. Estimates from the UMD/MODIS and CERES models at 1^0 resolution are summarized in Table 4 while those from UMD/MODIS, ISCCP/GISS and ISCCP/UMD/SRB at 2.5^0 resolution are presented in Table 4.11. The UMD/MODIS estimates at 1^0 resolution have the smallest bias, lowest RMSE, and highest correlation coefficient of 3.7 W/m^2, of 17.8.2 W/m^2 and 0.93, respectively. ISSCP/GISS and ISCCP/UMD/SRB underestimate the surface downward SW fluxes by 6% and 5% respectively while CERES overestimates them by 5%.

Table 4.11 Comparison of monthly mean surface downward SW fluxes from UMD/MODIS, ISCCP/GISS and ISCCP/UMD/SRB against ground measurements at CAMP stations. The mean of observations is 214.9 W/m^2 and there are 96 samples. (September 2002-August 2003)

Sources(Resolution)	Cor .Coef.	RMSE (%)	BIAS (%)
UMD/MODIS(1^0)	0.93	17.8 (8)	3.7 (2)
CERES(1^0)	0.89	23.4 (11)	10.71 (5)
ISCCP/GISS(2.5^0)	0.88	25.1 (12)	-12.0 (6)
ISCCP/UMD/SRB(2.5^0)	0.90	22.5.1 (10)	-9.9 (5)

4.2 Radiative fluxes from MODIS swath products

SW radiative fluxes at 5 km resolution over North America were generated from MODIS Level-2 swath products both from Terra and Aqua for the year 2003. The MODIS instrument has a viewing swath width of 2,330 km, so each 5 minutes

MODIS swath has a width of 1,354 km and a length of 2,030 km. Level 2 cloud (MOD06, MYD06), aerosol (MOD06, MYM06) and atmospheric profiles (MOD07, MYD07) are used to compute the radiative fluxes.

Cloud optical depth and cloud droplet effective radius at 1 km pixel resolution, cloud top pressure at 5 km pixel resolution are taken from the cloud swath product. Theoretically, the SW fluxes could be computed at the same resolution. However, at such high spatial resolutions, the heterogeneity effect due to optical depth variability and the horizontal transport effect of light moving between cloud columns, usually referred to as cloud 3-D effect, become pronounced. The 1-D radiative transfer models with the assumption of plane-parallel and homogeneous clouds neglect the cloud 3-D effects and subsequently, are unable to provide an accurate description of the radiation field at small scale (Barker and Davies, 1992; Cahalan et al., 1994; Loeb et al., 1998; Varnai, 2000). Since the new inference scheme does not account for the 3-D cloud effects, the radiative fluxes will be computed at 5 km resolution at which much of the 3-D cloud effects can be neglected. To get the cloud properties at 5 km, twenty five 1 km pixels were sorted into water cloud, ice cloud, and clear sky pixels (pixels of undetermined phase were treated as water cloud pixels) according to the phase information of pixels from "Primary Cloud Retrieval Phase Flag" stored in the dataset named as "Quality_Insurance_1km" of swath cloud products. For every cloud type, cloud fraction was given by the fraction of the corresponding type to the twenty five pixels. Cloud optical depth was calculated as a logarithmic mean and cloud droplet effective radius was computed as

an arithmetic average. Surface elevation at 5 km resolution is also provided in the swath cloud product.

Aerosol optical depth from Level 2 aerosol swath products is at 10 km resolution and is interpolated into 5 km... Precipitable water and total column ozone amount from level-2 atmosphere profile swath product are at 5 km resolution. Missing value of precipitable water and aerosol optical depth are filled with the same data sources as used in the implementation of the global daily product in Section 3. Spectral surface albedo at 0.05^0 longitude/latitude grid cells was taken from The Filled Land Surface Albedo Product as described in Section 4.1.1.

4.2.1 Results

Figure 4.13 shows an example of a swath of surface downward SW fluxes at 16:40, July 1, 2003 UTC time over the United Sates and a corresponding swath of a cloud image from MODIS onboard Terra. As evident, there was a tropical depression system sweeping over south eastern United States. A wide variety of cloud types was present; deep convective clouds in the Gulf of Mexico, cirriform clouds in the outer region of the depression, stratiform clouds to the west of the depression and cumulus and cumulonimbus clouds representing the depression system. The derived surface SW fluxes give a very fine structure of the radiation field resulting from the cloud systems, with large reduction of solar radiation by deep convective and thick cumuliform clouds and slight reduction by thin cirriform and stratifrom clouds.

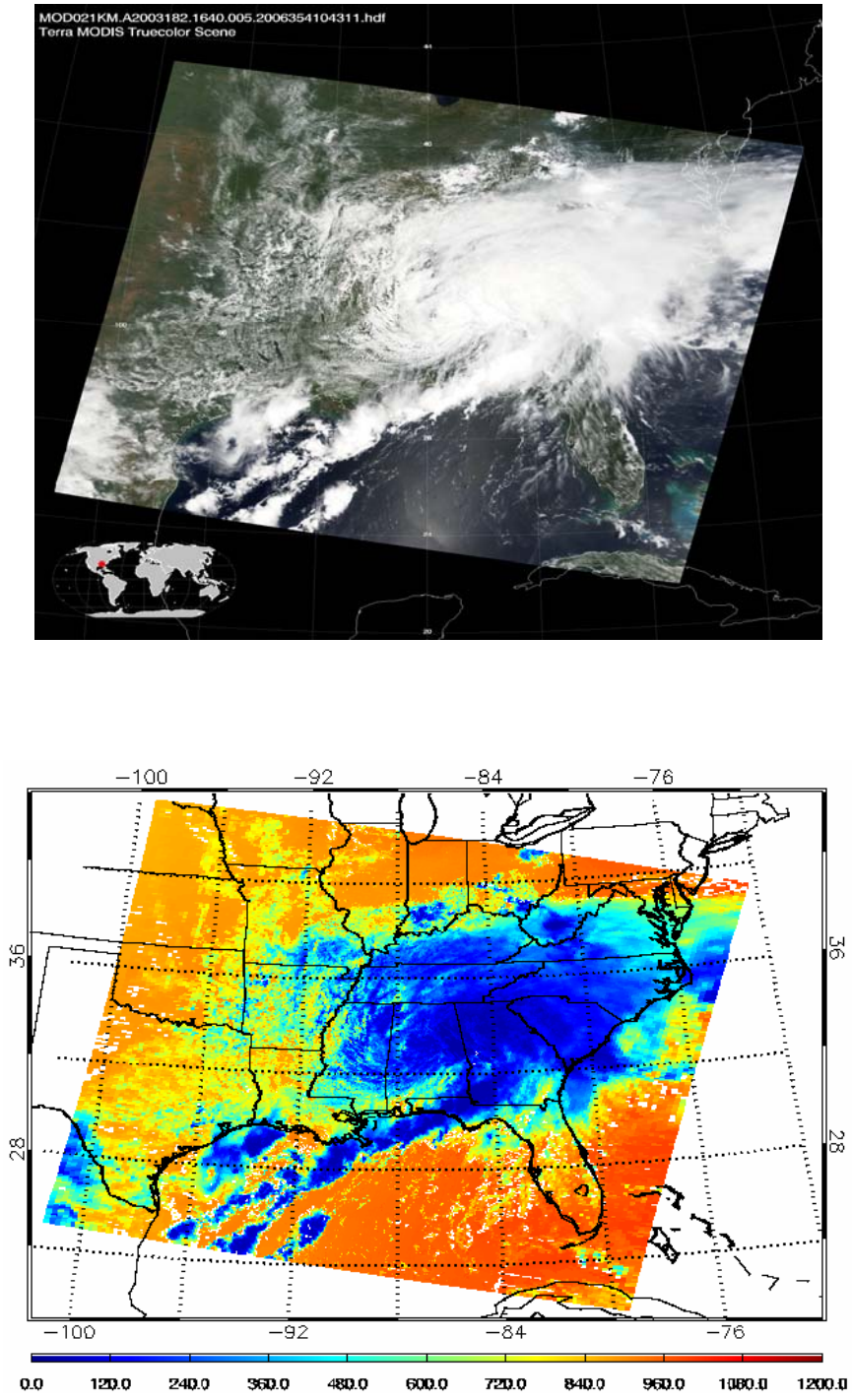

Figure 4.13 Example of surface downward SW flux at 5 km resolution and corresponding satellite cloud image at 16:40 UTC time on July 1, 2003

4.2.2 Evaluation

The ground measurements for the evaluation of the high resolution fluxes are taken from the ARM sites and from the Surface Radiation Network (SURFRAD) of NOAA (Augustine et al., 2000). Five sites of ARM, Central Facility, Extended Sites-1, 3, 18, and 22, are chosen. The downwelling SW flux from the ARM observations is the "sirs1butt" Value Added Product (VAP) of Solar and Infrared Radiation Station (SIRS) measurements with correction for diffuse irradiance. The observations are provided at 1-minute time interval. Six SURFRAD sites are: Bondville, IL, Boulder, CO, Desert Rock, NV, Fort Peck, MT, Goodwin Greek, MS and Penn State, PA. The total downwelling irradiance averaged for 3 minutes interval is calculated as the sum of direct and diffuse irradiance measured by pyranometers. To reduce large variance caused by broken cloud field, all the ground measurements were averaged over a 15 minute time window centered at MODIS overpass time.

Table 4.12 presents the evaluation results of surface downward SW fluxes at 5 km resolution at Terra overpass time. The results show that the estimated fluxes agree well with ground measurement. For the eleven sites chosen in this study, the relative bias ranges from 0 to 5%, the relative RMSE falls between 7 and 21% and the correlation coefficients are between 0.91 and 0.97. Due to the adjacency of the location and terrain similarity, all ARM sites show similar results except for site E-22 with a relatively large positive bias of 31 W/m^2 (5%). It is seen that this seemingly large bias is due to several outliers; if removed the bias will become negative similar to the other sites. Overall, the agreement of the satellite estimates with ground observations is better at the ARM sites than the SURFRAD sites. One reason might

be that for the ARM site, data quality is more strictly checked. Another possibility is the fact that the SURFRAD sites cover diverse geographic regions and MODIS retrievals might still need to be re-examination for some of them. If all sites are merged together, the correlation coefficient is 0.95, bias is about 3 W/m^2 (1), and the RMSE is 92 W/m^2 (15). The estimated fluxes at 5 km resolution are in much better agreement with ground measurements than the 1^0 latitude/longitude fluxes due to the improved scale matching (Pinker and Lazlo, 1991; Pinker et al., 2003; Li et al., 2005).

The estimated fluxes and their corresponding ground measurements are grouped into the four seasons (DJF, MAM, JJA and SON). Table 4.13 presents the evaluation results after merging all sites for the four seasons. As evident, the largest differences between estimated and observed fluxes are found during the winter season, with a correlation coefficient of 0.85, large negative bias of -28 W/m^2 (7%), and a RMSE of 108 W/m^2 (28%). The relatively large underestimation of fluxes in the winter season indicates that the disagreement might be due to the misidentification of snow as clouds in the MODIS products.

Similar evaluation was performed for surface downward SW fluxes at Aqua overpass time. Since the results are very similar to those from Terra as described above, they are not presented here.

Table 4.12 Evaluation results for surface downward SW flux at 5 km resolution against 15 minute averaged ground measurements at ARM and SURFRAD sites at MODIS overpass time (W/m^2)

	Mean Obs	Corr Coef	Bias (%)	RMSE (%)	# Obser
Central Facility	**603**	**0.94**	**-13 (2)**	**103 (17)**	**141**
E-1	**604**	**0.95**	**-13 (2)**	**93 (15)**	**141**
E-3	**585**	**0.96**	**-12 (2)**	**78 (13)**	**171**
E-18	**581**	**0.96**	**-12 (2)**	**77 (13)**	**141**
E-22	**634**	**0.96**	**31 (5)**	**78 (12)**	**126**
Desert Rock	**817**	**0.97**	**-20 (2)**	**60 (7)**	**104**
Penn State	**466**	**0.95**	**-15 (3)**	**98 (21)**	**112**
Bondville	**561**	**0.97**	**-3 (0)**	**75 (13)**	**112**
Goodwin Creek	**591**	**0.91**	**9 (2)**	**121 (20)**	**110**
Fort Peck	**524**	**0.93**	**-8 (2)**	**108 (21)**	**130**
Boulder	**681**	**0.92**	**26 (4)**	**111 (16)**	**115**
All sits	**601**	**0.95**	**-3 (1)**	**92 (15)**	**1403**

Table 4.13 Evaluation of instantaneous surface downward SW flux estimates at 5 km resolution against ground measurements at five ARM sites for different season (W/m^2)

Season	Mean Obs	Cor Coef	Bias (%)	RMSE (%)	# Obser
DJF	381	0.85	-28 (7)	108 (28)	221
MAM	657	0.97	8 (1)	78 (12)	333
JJA	749	0.92	5 (1)	103 (14)	436
SON	518	0.95	-8 (1)	82 (16)	413

To demonstrate the improvements attainable with the new inference scheme (UMD/MODIS), this version as well as version UMD/SRB_M are implemented with the same MODIS input products. The swath products over the United States from

July 1 to September 30, 2003 are used. Figure 4.14 shows the scatter plots of estimated surface downward SW fluxes from the two models against ground measurements at ARM sites. The new inference scheme reduces the RMSE from 95 to 88 W/m^2 and the bias from -22 to -12 W/m^2.

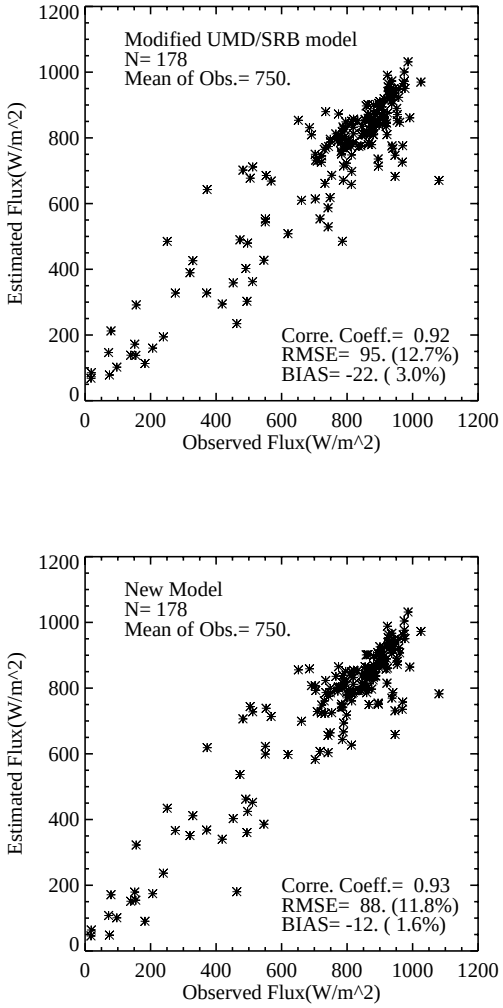

Figure 4.14 Evaluation of instantaneous surface downward SW fluxes at 5 km resolution from UMD/SRB_M model(Modified UMD/SRB) and UMD/MODIS model (New) against ground measurements at ARM sites at MODIS overpass time (July 1-September 30, 2003**)**

4.2.3 Spatial representativeness of point measurements

Difficulties in assessing the accuracy of radiative fluxes derived from satellites arise due to the temporal and spatial incompatibility of the two fluxes. Satellite based radiative fluxes typically cover a large area while ground measurements are at one location. This represents a limit to the ability to compare satellite retrievals and point measurements (Perez et al., 2001). The mean bias between satellite retrievals and ground measurements can be small, but the RMSE can be of the order of 20%. Moreover, the ground measurements are not always in the center of the satellite grid cell which adds additional complexity. Cloud patterns move over the ground sites and produce temporal variability in the measured radiative flux. Several studies on spatial and temporal variability of both ground measurements and satellite retrievals have investigated the spatial representativeness of ground measurements (Pinker et al., 1992, 2003; Li et al., 2003; Perez et al., 1997). Most of these studies focused on hourly and daily radiative fluxes.

The high spatial resolution radiative fluxes derived from MODIS observations provides a unique opportunity to investigate the spatial representativeness of ground measurements for the validation of instantaneous radiative fluxes based on satellites. To avoid complications due to snow conditions, the investigation is conducted for the time period from March 1 to November 30 of 2003. The study is focused on Southern Great Plains where ARM sites have similar geographic characteristics and experience same weather systems. Four ARM sites, Central Facility, E-1, E-3 and E-18 are chosen. As shown in Table 4.12, the comparison of estimated fluxes and ground measurements at those sites yields similar results. The measured surface downward

SW flux is averaged over time windows of 15, 30, 45, 60, 75 and 90 minutes centered at Terra overpass time. The estimated flux at different spatial scales was obtained by averaging values of all pixels falling into an area centered at ground sites and with a radius ranging from 5 to 100 km. The statistics between temporally averaged measurements and spatially averaged UMD/MODIS fluxes are computed. The results are sorted by season (MAM, JJA and SON).

Figure 4.15 shows the correlation coefficient, mean bias and RMSE as a function of spatial scale for different averaging time intervals for the Spring season. For each averaging time interval, as spatial scale increases, the RMSE falls at first and then rises at a point that varies with the averaging time intervals. For spatial scales smaller than 40 km, the RMSE decreases as the increase of averaging time interval, while for spatial scale greater than 40 km, the RMSE decreases at first and then increases after the averaging time scale became longer than 1 hour. The correlation coefficient exhibits similar pattern but changes in opposite direction. Since for a specific averaging time interval, the best correlation between ground measurement and satellite estimates is found at turning point of the statistics curve, the turning point can be considered as the representative spatial scale of one specific averaging time interval. The mean bias is quite small, no more than 1% relative to the mean of the observations.

In terms of spatial scale and averaging interval, in spring, the best correlation is found around spatial scale of 35 km and averaging interval of 60 minutes, with a

correlation coefficient of almost 0.99 and a RMSE of 46 W/m^2, which is approximately 8% relative to the observed mean.

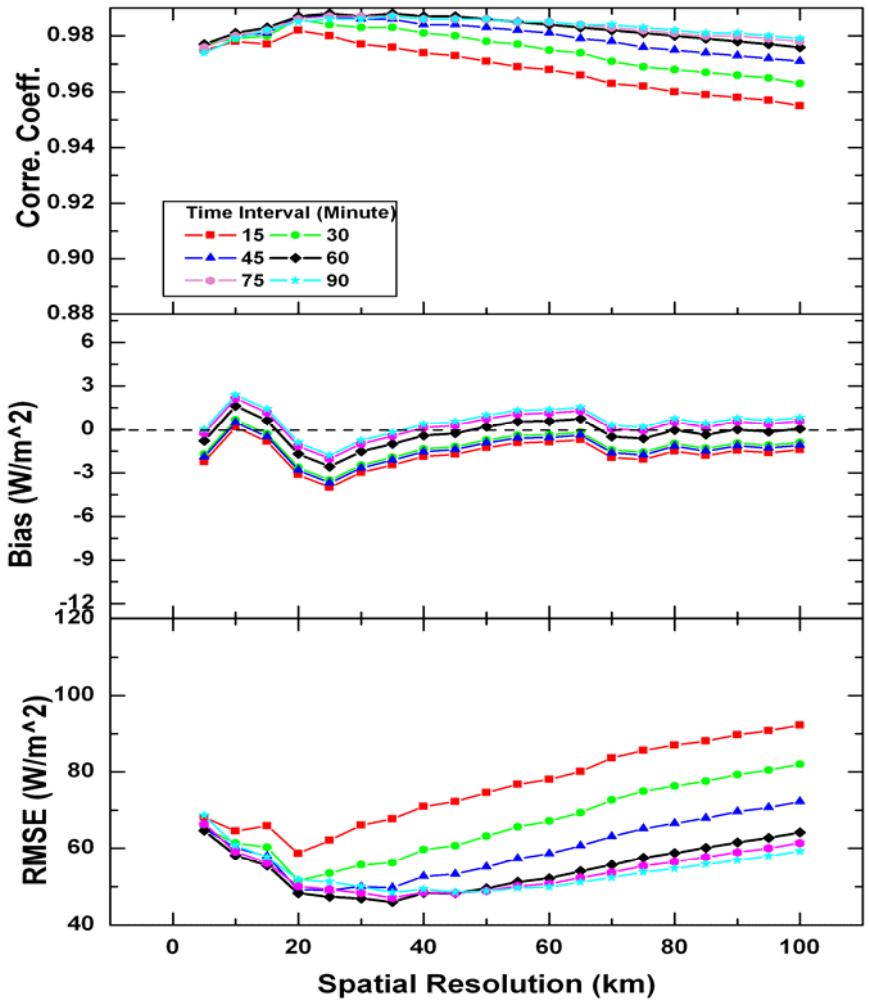

Figure 4.15 Statistics of differences between derived and observed fluxes as a function of spatial averaging scale for different temporal averaging intervals for the months of MAM, 2003

Figures 4.16 and 4.17 display the results for the summer months of JJA and the fall months of SON, respectively. Both seasons display similar dependence of

statistical values on spatial and temporal scales as was shown for spring. There are distinctive seasonal variations. For the summer month, the increase rate of correlation coefficient and decrease rate of RMSE with the increase of averaging time is greater than in spring. This indicates that the spatial variability of solar radiation is larger in summer than in spring. The turning point in the correlation and RMSE curves occurs around 25 km for one hour interval. As for the fall season, the dependence of correlation on spatial and temporal scales, illustrated in Figure 4.13, is weaker than in spring and summer. This can be explained by the cloud climatology in Southern Great Plains (Lazarus et al., 2000). Spring season has the highest cloud amount. While cloud amount is the lowest in summer, it has frequent cumuliform clouds of the broken type. This leads to larger spatial variability of radiative fluxes in the summer. The fall season has moderate amount of clouds of stratiform and cirriform type.

In general, ground measurements averaged for one hour agree best with satellite derived fluxes at scale around 20-40 km. It should be noted that all those findings were just based on ground measurements in Southern Great Plains. To get a broader view of spatial representativeness of ground measurements, the studies should be performed at ground stations in diverse climate zones and geographic regions.

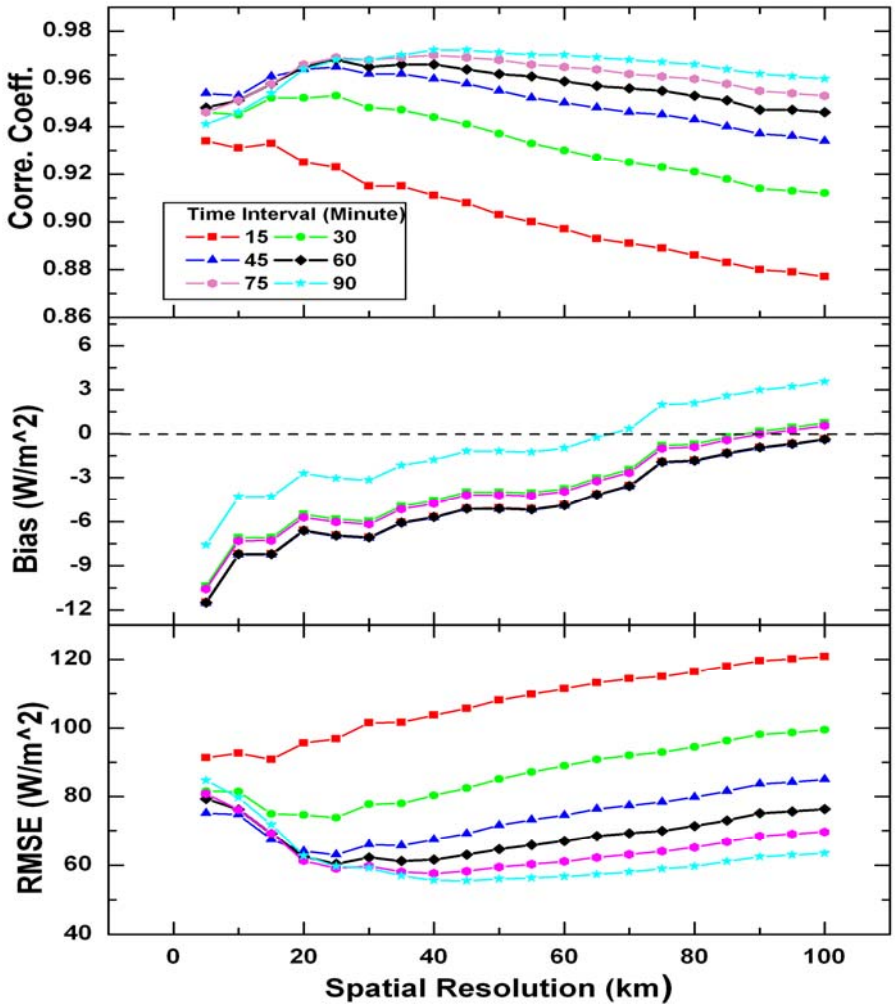

Figure 4.16 Statistics of differences between derived and observed fluxes as a function of spatial averaging scale for different temporal averaging intervals for the months of JJA, 2003

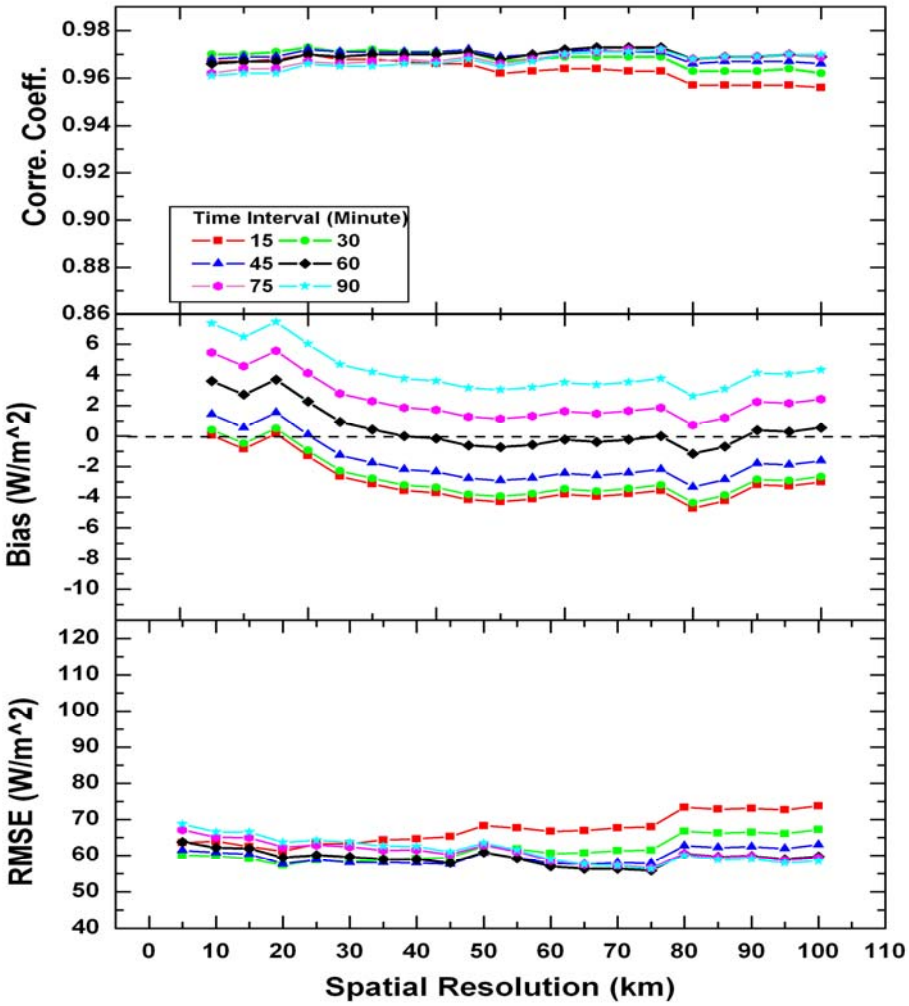

Figure 4.17 Statistics of differences between derived and observed fluxes as a function of spatial averaging scale for different temporal averaging intervals for the months of SON, 2003

4.3 Photosynthetically Active Radiation (PAR)

Information on Photosynthtically Active Radiation (PAR) (0.4-0.7 μm), is needed at different spatial scales for applications dealing with biogeochemical processes such as net primary productivity and ecosystem modeling (Running et al.,

1999; Platt, 1986; Prentice et al., 1992). Ground measurements of PAR are very limited. There are far fewer ground stations measuring PAR than total SW radiation. Satellite observations are the only sources for providing consistent information on PAR. MODIS observations have been applied to estimate PAR using simplified radiative transfer models over land and over oceans (Van Laake and Sanchez-Azofeifa, 2004; Carder et al., 1999). Those simplified models are limited in their capability to deal with multiple scattering by clouds and aerosol and lack transferability to global scale.

When implemented with MODIS products as described in Section 4.2, the UMD/MODIS model can estimate SW radiative fluxes in several spectral intervals, one of which is the PAR region. Computed are surface downward, surface upward and surface downward diffuse PAR. Figure 4.18 shows an example of instantaneous surface downward PAR over North America at Terra overpass time on Jul 1, 2003 at 5 km spatial resolution.

The derived surface downward PAR at 5 km resolution over North America at Terra and Aqua overpass time was evaluated with measured PAR averaged over 15 minutes at the same six SURFRAD sites as described in Section 4.2. Figure 4.19 shows the scatter plot of MODIS based estimates and measured PAR values for 2003, when all sites are combined. The PAR estimates agree well with ground measurements, with a correlation coefficient of 0.95, a bias of 3 Wm^2 (1%), and a RMSE of 42 W/m^2 (16%). Statistics for individual sites are listed in Table 4.14 giving an RMSE from 24 (7%) to 50 (22%) W/m^2, with a bias that varies from 1

(0%) to 16 W/m^2 (7%). Lack of spatial representativeness of point measurements contributes to part of the disagreement between observed and derived PAR. By averaging ground measurements over a longer time period and satellite derived PAR for a larger area, both RMSE and bias are reduced.

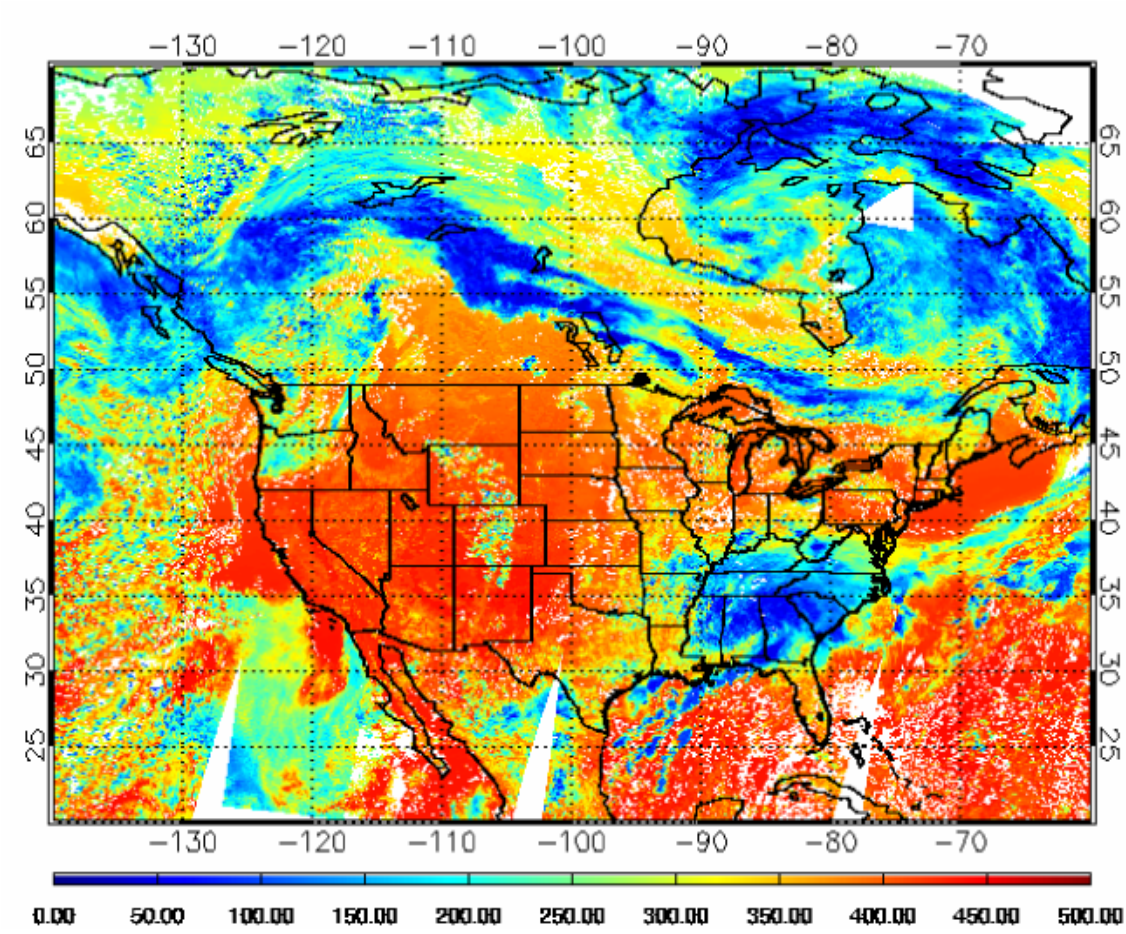

Figure 4.18 Surface downward PAR at 5 km resolution over North America at 10:30 local time on July 1, 2003

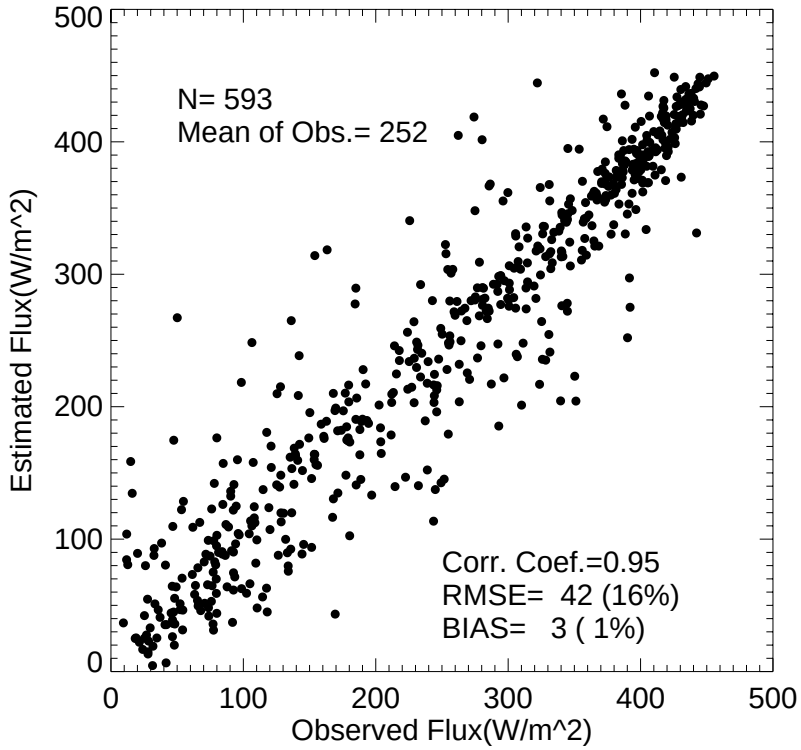

Figure 4.19 Scatter plot of surface downward PAR against ground measurements at six SURFRAD sites for 2003

Table 4.14 Evaluation of surface downward PAR against ground measurements from six SURFRAD sites for 2003

Sites	**Mean of Observation (W/m^2)**	**Correlation Coefficient**	**Bias (%) (W/m^2)**	**RMSE (%) (W/m^2)**	**Number of Observation**
Desert Rock	353	0.97	-1 (0)	24 (7)	94
Penn State	192	0.94	1 (0)	42 (22)	104
Bondville	226	0.97	12 (5)	36 (16)	99
Goodwin Creek	238	0.94	16 (7)	45 (19)	86
Fort Peck	225	0.92	-10 (4)	50 (22)	115
Boulder	296	0.92	8 (3)	49 (16)	95
All sits	253	0.95	4 (1)	42 (17)	593

Chapter 5: Summary and Conclusions

A new inference scheme was developed (UMD/MODIS) for utilizing information from the MODIS instruments on the Terra and Aqua satellites, to estimate spectral SW radiative fluxes. The scheme can be implemented at various spatial scales and as such, respond to existing voids in current information on shortwave radiative fluxes. It is based on the heritage of the UMD/SRB modeling activity and utilizes the most recent parameterizations of clouds, aerosols, and water vapor and it can resolve the vertical variability of the radiative fluxes. The new inference scheme deals with both water and ice clouds, considers the variation of cloud droplet radius, takes into account the spectral variation of cloud optical properties and water vapor absorption in the near infrared spectrum, and allows for the correction of surface elevation effects. Evaluation of the new scheme against a high resolution complex radiative transfer model demonstrated that the UMD/MODIS inference scheme has the required accuracy in computing SW radiative fluxes. The new model is implemented with MODIS products and compared with ground measurements.

Specifically, the UMD/MODIS model was implemented with MODIS global daily products for a period of one year (2003). The daily average values constructed from the combination of Terra and Aqua agree well with ground measurements. An extensive dataset of global SW radiative fluxes was generated for the first time exclusively based on MODIS observations. In addition to SW radiative fluxes at the surface and at the TOA, vertical profiles are also produced. Compared to other satellite datasets, improvement in the estimates of the SW radiative fluxes at the

surface were achieved at most of the available high quality BSRN sites. The improvement is very significant at problematic areas for most inference schemes such as the Tibet Plateau and Antarctica. The results indicate that with the combination of Terra and Aqua, it is possible to account for diurnal variations.

The spectral SW radiative fluxes at 5 km resolution over North America are as derived from the MODIS swath products are also in good agreement with ground observations and meet the need for high resolution information for hydrological and biogeochemical modeling. The 5 km SW radiative fluxes derived from both Terra and Aqua are already being utilized in hydrological studies at basin scale.

The availability of SW fluxes at 5 km resolution provides an opportunity to assess optimal matching between ground and satellite observations since the correlation between spatially averaged and temporally averaged fluxes can be investigated. It was found that the highest correlation is found to be between observations averaged over one hour and satellite derived fluxes at 20 to 40 km scale. This suggests that the derived flux at 20 to 40 km resolution could be used to represent the one hour averaged ground measurements. The high resolution flux from MODIS can be instrumental in validating other satellite datasets in remote regions where ground observations are unavailable.

To further improve the accuracy of radiative fluxes derived from MODIS products, some outstanding issues need to be addressed. An extensive error analysis needs to be carried out to identify the major error sources of UMD/MODIS model.

Errors caused by uncertainties of satellite retrievals for different atmospheric and surface need to be used to evaluate the radiative transfer part of UMD/MODIS model. The uncertainties brought forth by using plane parallel assumptions to compute radiative fluxes at high spatial resolution will be assessed with a 3-D radiative transfer model.

The Level-3 global products were generated from aggregation and sub-sampling of every fifth pixel of Level-2 swath products. The sub-sampling might result in errors in the mean cloud optical depth and cloud effective radius (Orepoulos, 2005). Moreover, due to nonlinearity of radiative fluxes to atmospheric properties, errors might be introduced by using averaged atmospheric properties to compute radiative flux. Although the combination of Terra and Aqua provides satisfactory daily average, two observations are not adequate to represent the diurnal cycle in regions where there are large diurnal variations. The diurnal variation information from geostationary satellites will be considered and incorporated in the computation of daily averages.

The evaluation results from the implementation of the new inference scheme with MODIS observations demonstrate the readiness of the new scheme to use new information that will be coming from new observations. The A-train satellite constellation consists of six Sun synchronous satellites (Earth Observing System Aqua and Aura, CLOUD SATellite (CloudSat), Cloud-Aerosol Lidar and Infrared Pathfinder Satellite Observation (CALIPSO), Polarization and Anisotropy of Reflectances for Atmospheric Science coupled with Observations from a LIDAR

(PARASOL) and the Orbiting Carbon Observatory (OCO). The advanced instruments and measurements of the A-train constellation should provide improved information on clouds and aerosols. The new inference scheme possesses the flexibility to be applied with observation from the new generation of satellites. A better understanding of solar radiation budget is anticipated through the implementation of the new inference scheme with such observations.

Publications and presentations resulting from work:

Wang, H, Takashi Y., Nakajima, Alkiko Higurashi, Teruyuki Nakajima, et al., 2002. A New Approach to Estimate Surface Short-Wave Fluxes over the Oceans. Spring AGU, Washington, DC, May 28-June 1.

Pinker, R., Wang, H., King, M., and Platnick, S., 2003. First Use of MODIS Data to Cross-Calibrate with GEWEX/SRB Data Sets. *GEWEX NEWS*, Vol 13, No.4, 4-5

Wang, H., Pinker, R., and Laszlo, I., 2004. Evaluation of the GCIP/GAPP Short-Wave Surface Radiation product against independent satellite observations. Spring AGU, Montreal, Canada, May 17-21, 2004.

Pinker, R. T., Wang, H., 2005. Challenges of Accurate Representation of Radiative Forcing in Northern Eurasia. Pre-symposium GOFC-GOLD Workshop, 31st International Symposium on Remote Sensing of Environment, June 18 - 19, 2005, St Petersburg, Russia

Pinker, R. T., M. Wonsick, and H. Wang, 2005. Issues in Transferability of Inference Schemes for Radiative Forcing Functions under the CEOP Initiative. 5th International Scientific Conference on the Global Energy and Water Cycle, Orange County, California, June 20-24, 2005.

Wang, H., R. T. Pinker, and P. Minnis, 2007. Satellite Estimates of Surface Short-Wave Fluxes: Issues of Implementation. In revision, JTECHO.

Acronyms

ARM	Atmospheric Radiation Measurement
ATRAD	Atmospheric Radiation
AVHRR	Advanced Very High Resolution Radiometer
AWS	Automatic Weather Station
BSRN	Baseline Surface Radiation Network
CALIPSO	Cloud-Aerosol Lidar and Infrared Pathfinder Satellite Observation
CAMP	Asia-Australia monsoon project
CCN	Cloud Condensation Nuclei
CEOP	Coordinated Enhanced Observing Period
CERES	Clouds and Earth's Radiant Energy System
CloudSat	CLOUD SATellite
CSE	Continental Scale Experiment
DISORT	Discrete Ordinate Model
ERBE	Earth Radiation Budget Experiment
FOV	Field of Views
GCM	General Circulation Models
GEOS	Geostationary Operational Environmental Satellite
GEWEX	Global Energy and Water Cycle Experiment
GISS	Goddard Institute for Space Studies
GOCART	Global Ozone Chemistry Aerosol Radiation Transport
GPCP	Global Precipitation Climatology Project
GVaP	Global water Vapor Project
HITRAN	High-Resolution Transmission Molecular Absorption
IPCC	International Panel of Climate Change
ISCCP	International Satellite Cloud Climatology Project
ISLSCP	International Satellite Land Surface Climatology Project
ITCZ	Inter-Tropical Convergence Zone
LIDAR	Light Detection and Ranging

LWP	Liquid Water Path
LWC	Liquid Water Content
MODIS	Moderate Resolution Imaging Spectroradiometer
MM5	Mesoscale Model
MWIR	Mid-Wave Infrared
NCAR	National Center for Atmospheric Research
NASA	National Aeronautics and Space Administration
NCDC	National Climate Data Center
NCEP	National Centers for Environmental Prediction
NESDIS	National Environmental Satellite Data and Information Service
NIR	Near-Infrared
NOAA	National Oceanic and Atmospheric Administration
NWIR	Mid-Wave Infrared
NWP	Numerical Weather Prediction
OCO	Orbiting Carbon Observatory
OPAC	Optical Properties of Aerosols and clouds
PAR	Photosynthetically Active Radiation
PARASOL	Polarization and Anisotropy of Reflectances for Atmospheric Science coupled with Observations from a LIDAR
PBL	Planetary Boundary Layer
PSU	Penn State University
RICC	Regional Impacts of Climate Change
RMSE	Root Mean Spare Error
SAGE	Stratospheric Aerosol and Gas Experiment
SBDART	Santa Barbara Discrete ordinate Atmospheric Radiative Transfer Model
SGP	Southern Great Plains
SIRS	Solar and Infrared Radiation Station
SRB	Surface Radiation Budget
SSM/I	Special Sensor Microwave/Imager
SURFRAD	Surface Radiation Network

SW	Short Wave
SWIR	Short-Wave Infrared
TIROS	Television and Infrared Observation Satellite
TOA	Top of Atmosphere
TOMS	Total Ozone Mapping Spectrometer
TOVS	TIROS Operational Vertical Sounder
UMD	University of Maryland
VAP	Value Added Product
VISST	Visible-Infrared-Solar Infrared-Split
WCRP	World Climate Research Programme

References

Ackerman, S. A., Strabala, K., Menzel, P., Frey, R., Moeller, C., Gumley, L., Baum, B., Seeman, S. W., and Zhang, H., 1998. Discriminating clear-sky from cloud with MODIS: algorithm theoretical basis document (MOD35). *J. Geo. Res. Atmos.* V.103, Dec. 27, 1998.

Augustine, J. A., J. J. DeLuisi, and C. N. Long, 2000. SURFRAD-A National Surface Radiation Budget Network for Atmospheric Research, Bull. of Amer.Met. Soc. Vol. 81, No. 10, pp. 2341-2358.

Barnett, T.P., J. Ritchie, J. Foat, and G. Stokes, 1998. On the Space–Time Scales of the Surface Solar Radiation Field. *J. Climate*, *11*, 88–96.

Barker H. W., and J. A. Davies, 1992a. Cumulus cloud radiative properties and the characteristics of satellite radiance wavenumber spectra. *Remote Sens. Environ.*, *42*, 51–64

Barker, H. W., G. L. Stephens, P. T. Partain, J. W. Bergman, B. Bonnel, K. Campana, E. E. Clothiaux, S. Clough, S. Cusack, J. Delamere, J. Edwards, K. F. Evans, Y. Fouquart, S. Freidenreich, V. Galin, Y. Hou, S. Kato, J. Li, E. Mlawer, J.-J. Morcrette, W. O'Hirok, P. Raisanen, V. Ramaswamy, B. Ritter, E. Rozanov, M. Schlesinger, K. Shibata, P. Sporyshev, Z. Sun, M. Wendisch, N. Wood, and F. Yang, 2003. Assessing 1D atmospheric solar radiative transfer models: Interpretation and handling of unresolved clouds. *J. Climate*, *16***,** 2676-2699.

Bossel, H., 1996. TREEDYN3 forest simulation model. Ecological Modeling 90, pp. 187-227.

Carder, K., R. Chen, and S. Hawes, 2003. Instantaneous photosynthetically available radiation and absorbed radiation by phytoplankton MODIS Ocean Science Team Algorithm Theoretical Basis Document,ATBD MOD-20, version 7, 24 pp., NASA Goddard Space Flight Cent.,Greenbelt, Md.,

Cahalan R. F., W. Ridgway, and W. J. Wiscombe, 1994. Independent pixel and Monte Carlo estimates of the stratocumulus albedo. *J. Atmos. Sci.*, **51**, 3776–3790.

Cess, R. D., G. L. Potter, J. P. Blanchet, G. J. Boer, S. J. Ghan, J. T. Kiehl, H. Le Treut, Z.-X. Li, X.-Z. Liang, J. F. B. Mitchell, J.-J. Morcrette, D. A. Randall, M. R. Riches, E. Roeckner, U. Schlese, A. Slingo, K. E. Taylor, W. M. Washington, R. T. Wetherald, and I. Yagai, 1989.Interpretation of cloud-climate feedback as produced by 14 atmospheric general circulation models. *Science*, *245*, 513-516.

Charlson, R., et al., 1992. Climate forcing by anthropogenic aerosols, *Science*, *255*, 423–430.

Chen, F., K. Mitchell, J. Schaake, Y. Xue, H. Pan, V. Koren, Q. Duan, and A. Betts, 1996. Modeling of land surface evaporation by four schemes and comparison with FIFE observations, *J. Geophys. Res*., *101*, 7521-7268.

Chen S. S., and R. A. Houze, 1997. Diurnal variation and life-cycle of deep convective systems over the tropical Pacific warm pool. *Quart. J. Roy. Meteor. Soc*, 123, 357–388.

Chylek, P., and J. Coakley, 1974. Aerosols and climate, *Science*, *183*, 75–77.

Chylek, P., and J. Wong, 1995. Effect of absorbing aerosols on global radiation budget, *Geophys. Res. Lett*, *22*, 929–931.

Darnell W. L., W. F. Staylor, S. K. Gupta, N. A. Ritchey, and A. C. Wilber, 1992. Seasonal variation of surface radiation budget derived from ISCCP-C1 data. *J. Geophys. Res*, **97**, 15741–15760.

Dickinson, R., 1986. Global climate and its connection to the biosphere, In Climate-Vegetation Interactions, Rosenzweig, C. and R. Dickinson (eds.), 1986. *Proceedings of a workshop held at NASA/Goddard Space Flight Center, Greenbelt, MD*, January 27-29, 1986, p. 5-8.

Dubayah, R. and Rich, P. M., 1995. Topographic solar radiation models for GIS. *International Journal of Geographic Information Systems* 9: 405-19

Dubayah, R., Loechel, 1997. S. Modeling Topographic Solar Radiation Using GOES Data. *Journal of Applied Meteorology* 36: 141-154

Duvel J. P., 1989. Convection of tropical Africa and the Atlantic Ocean during northern summer. Part I: Interannual and diurnal variations. *Mon. Wea. Rev*, 117, 2782–2799.

Eric G. Moody, Michael D. King, Steven Platnick, Crystal B. Schaaf, and Feng Gao. 2005. Spatially Complete Global Spectral Surface Albedos: Value-Added Datasets Derived From Terra MODIS Land Products. IEEE TRANSACTIONS ON GEOSCIENCE AND REMOTE SENSING, VOL. 43, NO. 1, PP. 144-158.

Flowers, E. C., and E. L. Maxwell, 1986. Characteristics of network measurements. *Sol. Cells, 18***,** 205–212..

Garrat, J. R., P. B. Krummel, and E. A. Kowalczyk, 1993. The surface energy balance at local and regional scales-A comparison of general circulation model results with observations, *J. Climate, 6,* 1090-1109.

Grassl, H., 2002. CEOP-Global Monitoring for Improved Prediction. *CEOP Newsletter* No. 2.

Gray W. M., and R. W. Jacobson, 1977. Diurnal variation of deep cumulus convection. *Mon. Wea. Rev*, 105, 1171–1188.

Gu L. H., Baldocchi D., Verma S.B., Black T. A., Vesala T., Falge E. M. & Dowty P. R., 2002. Advantages of diffuse radiation for terrestrial ecosystem productivity. *Journal of Geophysical Research-Atmospheres 107*(D6), 4050, doi: 10.1029/2001JD001242.

Gupta, S. K., N. A. Rithey, A. C. Wilber, C. H. Whitlick, G. G. Gibson, and P. W. Stackhouse Jr., 1999. A climatology of surface radiation budget derived from satellite data. *J. Climate*, 12, 2691-2710

Gupta, S. K., Kratz, D. P., Stackhoue, P.W., Wilber, A. C., 2001. The Langley parameterized shortwave algorithm (LPSA) for surface radiation budget studies, NASA TP-2001-211272

Higurashi, A., and T. Nakajima, 1999. Development of a two channel aerosol retrieval algorithm on global scale using NOAA/AVHRR, *J. Atmos. Sci.*, 56, 924-941

Henderson-Sellers, A., 1993. The project for intercomparison of land-surface parameterization schemes, *Bull. Amer. Meteor. Soc*., 74, 1335-1350.

Holland, M.M. and C.M. Bitz, 2003. Polar amplification of climate change in coupled models, Clim. Dyn, 21,221-232, doi:00382-003-0332-6.

IPCC, 1998. The Regional Impacts of Climate Change: An Assessment of Vulnerability. Special Report of IPCC Working Group II [Watson, R.T., M.C. Zinyowera, and R.H. Moss (eds.)]. Intergovernmental Panel on Climate Change, Cambridge University Press, Cambridge, United Kingdom and New York, NY, USA, 517 pp.

Joseph, J., W. Wiscombe, and J. Weinman, 1976. The Delta-Eddington Approximation for Radiative Flux Transfer. *J. Atmos. Sci.*, 33, 2452–2459.

Kalnay, E. and Coauthors, 1996. The NCEP/NCAR Reanalysis 40-year Project. Bull. Amer. Meteor. Soc., 77, 437-471.

Kasabbova, T., R. T. Pinker, D. Goodrich, T. Keefer, A. Huete, and J. Privette, 2002. Evaluation of satellite based estimates of surface albedo with ground and aircraft observations in a semi-arid region. Spring AGU, Washington, DC, May 28-June 1, 2002.

Key, J., D. Santek, C.S. Velden, N. Bormann, J.-N. Thepaut, L.P. Riishojgaard, Y. Zhu, and W.P. Menzel, 2002. Cloud-drift and Water Vapor Winds in the Polar Regions from MODIS, IEEE Trans. Geosci. Remote Sensing, 41(2), 482-492.

King, M. D., Kaufman, Y. J., Menzel, W. P., and Tanré, D., 1992. Remote sensing of cloud, aerosol, and water vapor properties from the Moderate Resolution Imaging Spectrometer (MODIS). *IEEE Transactions on Geoscience and Remote Sensing, 30*, 2-27.

King, M. D., W. P. Menzel, Y. J. Kaufman, D. Tanré, et al., 2003. Cloud and Aerosol Properties, Perceptible Water, and Profiles of Temperature and Humidity from MODIS**.** *IEEE Trans. Geosci. Remote Sens*., *41***,** 442-458.

Lazarus, S. M., S. K. Krueger, and G. G. Mace, 2000. A Cloud Climatology of the Southern Great Plains ARM CART. *J. Climate*, *13*, 1762–1775.

Leigh Jr., E. G., 1999. Tropical forest ecology: A view from Barro Colorado Island., Oxford University Press, New York, NY

Li, X., R. T. Pinker, M. M. Wonsick, and Yingtao Ma, 2006. Towards improved satellite estimates of short-wave radiative fluxes: Focus on cloud detection over snow. 1. Methodology: J. Geophys. Res., Vol. 112, No. D7D0720810.1029/2005JD006698

Li, Z., L. Moreau, A. Arking, 1997. On solar energy disposition, a perspective from observation and modeling, *Bull. Amer. Meteor. Soc*., 78, 53-70

Li, Z., and H. G. Leighton, 1993. Global climatology of solar radiation budget at the surface and in the atmosphere from 5 years of ERBE data. *J. Geophys. Res*., 98, 4919-4930

Li, Z., M. C. Cribb, F.-L. Chang, A. Trishchenko, and Y. Luo, 2005. Natural variability and sampling errors in solar radiation measurements for model validation over the Atmospheric Radiation Measurement Southern Great Plains region, *J. Geophys. Res.*, 110, D15S19, doi:10.1029/2004JD005028.

Liu, H., R. T. Pinker and B. N. Holben, 2004. A global view of aerosols from merged transport models, satellite and ground observations. J. Geophys. Res., Vol. 110, No. D10, D10S1510.1029/2004JD004695.

Liu, H., R. T. Pinker, M. Chin, B. Holben and L. Remer 2007. Aerosol Optical Properties at Global Scale. JGR-Atmospheres, in revision.

Loeb N. G., T. Várnai, and D. M. Winker, 1998. Influence of subpixel-scale cloud-top structure on reflectances from overcast stratiform cloud layers. *J. Atmos. Sci.*, *55***,** 2960–2973.

Lohmann, U., and G. Lesins, 2002. Stronger constrains on the anthropogenic indirect aerosol effect, *Science*, *298*, 1012–1015.

Lucht, W., C. B. Schaaf, and A. H. Strahler, 2000. An Algorithm For the Retrieval of Albedo from Space Using Semi-empirical BRDF Models. *IEEE Trans. Geosci. Remote Sens., 38***,** 977-998.

Masuda, K., 2004. Surface radiation budget: comparison between global satellite-derived products and land-based observations in Asia and Oceania. International Radiation Symposium 2004, Busan, Korea, 2004

Meador, W., and W. Weaver, 1980. Two-Stream Approximations to Radiative Transfer in Planetary Atmospheres: A Unified Description of Existing Methods and a New Improvement. *J. Atmos. Sci.*, 37, 630–643.

Minnis, P., Kratz, D. P.; Coakley, J. A., Jr.; King, M. D.; Garber, D.; Heck, P.; Mayor, S.; Young, D. F. and Arduini, R., 1995. Cloud Optical Property Retrieval (Subsystem 4.3). "Clouds and the Earth's Radiant Energy System (CERES) Algorithm Theoretical Basis Document, Volume III: Cloud Analyses and Radiance Inversions (Subsystem 4)", *NASA RP 1376 Vol. 3*, edited by CERES Science Team, December, 1995, pp.135-176.

Minnis, P., W. L. Smith, Jr., D. F. Young, L. Nguyen, A. D. Rapp, P. W. Heck, and M. M. Khaiyer, 2002. "Near-real-time retrieval of cloud properties over the ARM CART area from GOES data." *Proc. 12th ARM Science Team Meeting, April 8-12, St. Petersburg, FL, 7 pp.*

Nakajima, T. Y., and T. Nakajima, 1995. Wide area determination of cloud microphysical properties from FIRE and ASTEX regions, *J. Atmos. Sci*., 52, 4043-4059.

Ohmura A., E. Dutton, B. Forgan, C. Frohlich, H. Gilgen, H. Hegne, A., Heimo, G., Konig-Langlo, B. McArthur, G. Muller, R. Philipona, C. Whitlock, K. Dehne, and M. Wild, 1998. Baseline Surface Radiation Network (BSRN/WCRP): New precision radiometery for climate change research. Bull. Amer. Meteor. Soc., Vol. 79, No. 10, 2115-2136.

Oreopoulos, L., 2005. The impact of subsampling on MODIS Level-3 statistics of cloud optical thickness and effective radius, *IEEE trans. geosci. remote sens. 43*(2), 366-373 (February 2005), DOI: 10.1109/TGRS.2004.841247.

Parslow, J. S., and G. P. Harris, 1990. Remote sensing of marine photosynthesis, Ecological Studies, Analysis and Synthesis. Vol. 79, R. J. Hobbs and H. A. Mooney, Eds., 312 pp.

Penner, J., R. Dickinson, and C. O'Neill, 1992. Effects of aerosols from biomass burning on the global radiation budget, *Science*, *256*, 1432–1434.

Perez R., Seals R., Zelenka A., 1997. Comparing satellite remote sensing and ground network measurements for the production of site/time specific irradiance data, Solar Energy, 60, 89-96.

Perez R., Kmiecik m., Zelenka A., Renne D., George R., 2001. Determination of the Effective Accuracy of Satellite-Derived Global, Direct and Diffuse Irradiance in the Central United States, Proceedings of the 2001 Annual Conference, of the American Solar Energy Society, 2001

Pinker, R. and J. Ewing, 1985. Modeling surface solar radiation: Model formulation and validation. J. Climate Appl. Meteor., 24, 389-401.

Pinker, R. T. and I. Laszlo, 1992. Modeling surface solar irradiance for satellite application on a global scale. *J. Appl. Meteor*., 31, 194-211.

Pinker, R. T., I. Laszlo, C. H. Whitlock and T. P. Charlock, 1995. Radiative Flux Opens New Window on Climate Research. *EOS,* 76, No. 15, April 11.

Pinker, R. T., J. D. Tarpley, I. Laszlo, K. E. Mitchell, et al., 2003. Surface Radiation Budgets in Support of the GEWEX Continental Scale International Project (GCIP) and the GEWEX Americas Prediction Project (GAPP), including the North American Land Data Assimilation System (NLDAS) Project. *J. Geophys. Res.*, 108 (D22), 8844, doi:10.1029/2002JD003301.

Pinker, R. T., Wang, H., King, M. D., Platnick, S., 2003. The First Use of MODIS Data to Cross-Calibrate with GEWEX/SRB Data Sets. *GEWEX NEWS*, Vol. 13, No. 4.

Pinker, R. T., Xu Li and Wen Meng, 2007. Towards improved satellite estimates of short-wave radiative fluxes: Focus on cloud detection over snow. Part II: Results. J. Geophys. Res., 112, D09204, doi:10.1029/2005JD006699.

Platnick, S., M. D. King, S. A. Ackerman, W. P. Menzel, B. A. Baum, J. C. Riédi, and R. A. Frey, 2003. The MODIS Cloud Products: Algorithms and Examples from Terra. *IEEE Trans. Geosci. Remote Sens.*, *41***,** 459-473.

Platt, T., 1986. Primary production of the ocean water column as a function of surface light intensity: Algorithms for remote sensing, *Deep Sea Res.,* 33, 149-163.

Poore, K., J. Wang, and W. B. Rossow, 1995: Cloud layer thicknesses from a combination of surface and upper-air observations. *J. Climate, 8,* 550–568.

Prentice, I. C., W. Cramer, S. P. Harrison, R. Leemans, R. A. Monserud, and A. M. Solomon, 1992. A global biome model based on plant physiology and dominance, soil properties, and climate, *J. Biogeog.,* 19, 117-134.

Ramanathan, V., E. J. Pitcher, R. C. Malone and M. L. Blackmon, 1983. The Response of a Spectral General Circulation Model to Refinements in Radiative Processes. *J. Atmos. Sci*., *40,*605-630.

Ramanathan, V., 1986. Scientific use of surface radiation budget data for climate studies. Surface Radiation Budget for Climate Application, J. T. Suttles and G. Ohring, Eds., *NASA Reference Publication* 1169, 58-86

Ramanathan, V., 1987. The Role of Earth Radiation Budget Studies in Climate and General Circulation Research. *J. Geophys. Res., 92*: 4075-4095.

Ramanathan, V., R. D. Cess, E. F. Harrison, P. Minnis, B. R. Barkstrom, E. Ahmad, and D. Hartmann, 1989. Cloud-Radiative Forcing and Climate: Results from the Earth Radiation Budget Experiment. *Science*, 243: 57-63.

Rind, D., C. Rosenzweig, G. R. Goldberg, 1992. Modeling the hydrological cycle in assessments of Climate Change. *Nature* 358 (6382), 119-122.

Rodell, M., P. R. Houser, U. Jambor, J. Gottschalck, K. Mitchell, C. J. Meng, K. Arsenault, B. Cosgrove, J. Radakovich, M. Bosilovich, J. K. Entin, J. P. Walker, D. Lohmann, and D. Toll, 2004. The Global Land Data Assimilation System. *Bull. Amer. Meteor. Soc.*, *85*, 381–394.

Rossow, W. B. and R. A. Schiffer, 1991. ISCCP Cloud Data Products. *Bull. Amer. Meteor. Soc*. *72***,** 2-20.

Rossow, W. B., and Y-C. Zhang, 1995. Calculation of surface and top-of-atmosphere radiative fluxes from physical quantities based on ISCCP datasets, Part II: Validation and first results. *J. Geophys. Res.*, 100, 1167-1197.

Rossow, W. B., A.W. Walker, D. E. Beuschel, and M. D. Roiter, 1996. International Satellite Cloud Climatology Project (ISCCP) Documentation of New Cloud Datasets. WMO/TD-No. 737, World Meteorological Organization, 115 pp.

Rossow W. B. and R. A. Schiffer, 1999. Advances in Understanding Clouds from ISCCP. *Bull. Amer. Meteor. Soc*., *80,* 2261-2287.

Running, S. W., 1990. Estimating terrestrial primary productivity by combining remote sensing and ecosystem simulation. Ecological Studies, Vol. 79, Remote Sending of Biosphere Functioning, R. J. Hobbs and H. A. Mooney, Springer-Verlag.

Running, S. W., Collatz, G. J., Washburne, J., S. Sorooshian, 1999. Land Ecosystems and Hydrology. *EOS Science Plan* 5:197- 260.

Schaaf, C. B., F. Gao, A. H. Strahler, W. Lucht, 2002. First Operational BRDF, Albedo and Nadir Reflectance Products from MODIS. *Remote Sens. Environ., 83***,** 135-148.

Sorooshian, S., 2003. GEWEX support reaffirmed at recent WCRP/JSC meeting. *GEWEX NEWS.* Vol. 13, No. 2, May 2003.

Stamnes, K., S. Tsay, W. Wiscombe and K. Jayaweera, 1988. Numerically stable algorithm for discrete-ordinate-method radiative transfer in multiple scattering and emitting layered media. *Appl. Opt., 27*, 2502-2509.

Stephens, G. L., 1978. Radiation profiles in extended water clouds. II: Parameterization schemes. *J. Atmos. Sci*., *35*, 2123-2132.

Stephens, G. L., S. Acherman, and E. Smith, 1984. A shortwave parameterization revised to improve cloud absorption. *J. Atmos. Sci*., *41*, 687-690.

Stephens, G, L., A. Slingo, M. J. Webb, P. J. Minnett, P. H. Daum, L. Kleinman, I. Wittmeyer, and D. A. Randall, 1994. Observations of the earth's radiation budget in relation to atmospheric hydrology. 4: Atmospheric column radiative cooling over the world's oceans. *J. Geophys. Res*. *99*, 18 585-18 604

Stroeve, J., M. M. Holland, W. Meier, T. Scambos, and M. Serreze 2007. Arctic sea ice decline: Faster than forecast, *Geophys. Res. Lett.*, *34*, L09501, doi:10.1029/2007GL029703.

Sui, C. -H., M. M. Rienecker, X. Li, K. -M. Lau, I. Laszlo, and R.T. Pinker, 2002. The impacts of daily surface forcing in the upper ocean over tropical Pacific: A numerical study. *J. Climate*, 16 (4): 756-766.

Sun, Z., K. P. Shine, 1995. Parameterization of ice cloud radiative properties and its application to the potential climatic importance if Mixed-Phase Clouds. *J. Climate* 8, 1874-1888

Tanaka, K., Ishikawa, H., Hayashi, T., Tamagawa, I. and Ma, Y., 2001. Surface Energy Budget at Amdo on the Tibetan Plateau using GAME/Tibet IOP98 Data, J. Meteo. Soc. Jpn, 79(1B), 505-517.

Twomey, S., 1977. The influence of pollution on the shortwave albedo oclouds, *J. Atmos. Sci.*, *34*, 1149–1152.

Van Laake, P. E. and Sánchez-Azofeifa, G. A. 2004. Simplified atmospheric radiative transfer modelling for estimating incident PAR using MODIS atmosphere products. Remote sensing of environment, 91 (2004)1, 98-113.

Várnai T., 2000. Influence of three-dimensional radiative effects on the spatial distribution of shortwave cloud reflection. *J. Atmos. Sci.*, *57*, 216–229

Wang, J., and W. B. Rossow, 1995. Determination of cloud vertical structure from upper-air observations. *J. Appl. Meteor., 34***,** 2243– 2258..

Wang, J., W. B. Rossow, and Y.-C. Zhang, 2000. Cloud vertical structure and its variation from 20-yr global radiosonde dataset*, J. Clim*., 12, 3041-3056.

Wang, X., and J. R. Key, 2005. Arctic surface, cloud, and radiation properties based on AVHRR Polar Pathfinder dataset: Part II. Recent trends. *J. Clim., 18,* 2575-2593

Wielicki, B.A., B.R. Barkstrom, E.F. Harrison, R.B. Lee, G. Louis Smith, and J.E. Cooper, 1996. Clouds and the Earth's Radiant Energy System (CERES): An Earth Observing System Experiment. *Bull. Amer. Meteor. Soc.*, **77**, 853–868.

Wielicki, B.A., Barkstrom, B.R., Baum, B.A., Charlock, T.P., Green, R.N., Kratz, D.P., Lee, R.B., Minnis, P., Smith, L.G., Wong, T., Young, D.F., Cess, R.D., Coakley, J.A., Crommelynck, D.A.H., Donner, L., Kandel, R., King, M.D.,

Miller, A.J., Ramanathan, 1998. Clouds and the Earth's Radiant Energy System (CERES): Algorithm Overview. *IEEE Transactions on Geosciences and Remote Sensing*, 36, 1127-1141

Wielicki B. A, A. D. Del Genio, T. M. Wong, J. Y. Chen, B. E. Carlson, R. P. Allan, F. Robertson, H. Jacobowitz, A. Slingo, D. A. Randall, J. T. Kiehl, B. J. Soden, C. T. Gordon, A. J. Miller, S. K. Yang, J. Susskind, 2002. Changes in tropical clouds and radiation Response, *Science*, 296 (5576): U2-U3.

Wild, M., A. Ohmura, H. Gilgen, and E. Roeckner, 1995. Validation of GCM simulated radiative fluxes using surface observations. *J. Climate*, 8, 1309-1324.

Wild, M., 2005. Solar radiation budgets in atmospheric model intercomparison from a surface perspective. Geophys. Res. Lett., Vol. 32, No. 7, L0770410.1029/2005GL022421

Wiscombe W. J., 1977. The delta-Eddington approximation for a vertically inhomogeneous atmosphere. Tech. Note TN-121+STR, National Center for Atmospheric Research, Boulder, CO, 66 pp.

Wylie, D. P., W. P. Menzel, H. M. Woolf, and K. L. Strabala, 1994. Four years of global cirrus cloud statistics using HIRS.. *J. Clim*., 7, 1972-1986.

Wood, E. F., D. P. Lettenmaier, X. Liang, B. Nijssen, and S. W. Wetzel, 1997. Hydrological modeling of continental scale basins, *Review of Earth and Planetary Sciences*, 25.

Yu, H., R. E. Dickinson, M. Chin, Y. J. Kaufman, et al., 2003. Annual Cycle of Global Distributions of Aerosol Optical Depth from Integration of MODIS Retrievals and GOCART Model Simulations, 2003. *J. Geophys. Res.*

Zhang, Y.-C., and A. A. Lacis, 1995. Calculation of surface and top of atmosphere radiative fluxes from physical quantities based on ISCCP data sets. 1: Method and sensitivity to input data uncertainty. *J. Geophys. Res*., 100, 1149-1165